FRONTAL PASSAGE AND COLD POOL DETECTION USING OKLAHOMA MESONET OBSERVATIONS

by

Andrew T. Lesage

A thesis submitted to the faculty of
The University of Utah
in partial fulfillment of the requirements for the degree of

Master of Science

Department of Atmospheric Sciences

The University of Utah

May 2013

The University of Utah Graduate School

STATEMENT OF THESIS APPROVAL

The thesis of **Andrew T. Lesage**

has been approved by the following supervisory committee members:

Steven K. Krueger	, Chair	**10/25/12** Date Approved
Edward J. Zipser	, Member	**10/25/12** Date Approved
Zhaoxia Pu	, Member	**10/25/12** Date Approved

and by **Kevin D. Perry**, Chair of the Department of **Atmospheric Sciences**

and by Donna M. White, Interim Dean of The Graduate School.

ABSTRACT

For over a dozen years the Oklahoma Mesonet network has provided surface observations at over 100 stations. These observations are used to analyze mass flux estimates from surface divergence, frontal passages, and cold pools, the latter defined herein as active regions where precipitation processes are creating near-surface cold air masses. Case studies are detailed and a 15-yr climatology of frontal passages and cold pools was computed in this research.

Convergence, divergence, and precipitation are most strongly correlated in the summer months and least correlated in the winter months. Wet spring and summer days had the highest average convergence and divergence values while dry summer and fall days had the lowest average convergence and divergence.

Frontal passages and cold pools are tracked throughout the Mesonet in various case studies, four of which are covered herein. The methodology is able to represent front location and cold pool areas quite well despite the low resolution of the Mesonet grid.

The climatology of front and cold pool data yielded many similarities. Winter has the largest magnitude changes in ΔT, ΔP, and Δh/cp while spring and fall had the largest magnitude change in Δq_v. Summer has the lowest with the exception of spring ΔT. Correlations between these variables are lowest in the more convectively active summer season. Convergence is roughly equal ahead of fronts from spring through fall; however, divergence is present in summer frontal passages earlier and stronger compared to the other seasons. Fronts and cold pools are most likely to occur in summer and spring with summer having the highest percentage of fronts which lead to cold pools. Fronts and cold pools are substantially more likely to occur during the late afternoon and early evening in the summer; other seasons had a slighter nocturnal increase in frequency. Western Oklahoma had higher frequencies of frontal

passages and cold pools than Eastern Oklahoma with frontal passages having the stronger signal.

These findings help identify seasonal, diurnal, and geographic distributions of fronts and cold pools and can be used in modeling studies to better the understanding of cold pool processes and parameterizations.

CONTENTS

LIST OF FIGURES

LIST OF TABLES

ACKNOWLEDGMENTS

This research was supported by the Office of Science (BER), U.S. Department of Energy, Grant No. DE-FG02-08ER64553.

Data were obtained from the Atmospheric Radiation Measurement (ARM) Program sponsored by the U.S. Department of Energy, Office of Science, Office of Biological and Environmental Research, Climate and Environmental Sciences Division. Gridded precipitation data was obtained from the National Weather Service Arkansas-Red Basin River Forecast Center. Radar images are from the University Corporation for Atmospheric Research (UCAR) image archive.

I would like to thank my committee members, Professor Edward Zipser, Dr. Zhaoxia Pu, and particularly my advisor Professor Steven Krueger for providing the opportunity to study and work on research at the University of Utah.

Finally I would like to thank my family and friends for their love and support.

CHAPTER 1

INTRODUCTION AND LITERATURE REVIEW

1.1 Oklahoma Mesonet Studies

The Oklahoma Mesonet dataset has been used in previous studies on convective systems such as MCSs and bow echoes.

A four-stage convective life cycle for a mesoscale convective system (MCS) was developed from Oklahoma Mesonet data from cases resulting in cold pools: 1) first storms, 2) MCS initiation, 3) mature MCS, and 4) MCS dissipation (Engerer et al., 2008). A mean potential temperature decrease of 9.5 K and a mean pressure increase of 4.5 mb was found for the first storms life cycle stage with these magnitudes of change dropping slightly throughout the rest of the life cycle. The station resolution of the Oklahoma Mesonet, roughly 40 km on average, is suitable enough to represent large MCS events and their associated cold pools. Smaller systems, such as a cold pool from an individual cumulonimbus cloud, can be missed in the Mesonet grid.

Oklahoma Mesonet data have also been used to find dozens of bow echo cases (Adams-Selin and Johnson, 2010). Adams-Selin and Johnson produced a conceptual model for the stages for bow echoes in their study, which is composed of four stages: 1) initial formation of the convective line, 2) the pressure surge, 3) new bowing, and 4) dissipation. These cases contain the characteristic pressure rise and temperature drop associated with cold pools.

With Oklahoma Mesonet data reaching back over a decade, this thesis determines mass flux estimates and identifies frontal passages and cold pools from Mesonet surface observations. Surface divergence values at Oklahoma Mesonet gridded triangles are calculated. These divergence values can be used as a proxy for updraft and downdraft mass fluxes and are compared to precipitation data from the Mesonet to

determine seasonality differences as well as differences in strength of convergence and divergence.

Frontal passages are determined using pressure and temperature differences at Mesonet stations. These variables are chosen for the analysis due to their use in other studies as well as temperature falls and pressure rises being a distinct feature of cold pools. Fronts and cold pools can be analyzed for the 1997-2011 dataset of Mesonet observations.

First, however, it is necessary to define a cold pool. Sections will follow on various types of studies on convective systems and features that influence or are influenced by cold pools: outflow boundaries, squall lines and bow echoes, and mesoscale convective systems (MCSs). The final section focuses on studies involving parameterizations related to cold pools and convective processes.

1.2 Defining a Cold Pool

Cold pools are a prominent and common feature of convective storms that have been studied for over half a century. Observations from the Thunderstorm Project showed evaporative cooling leading to descent in the region behind a squall line (Newton, 1950). Convergence ahead of the leading edge of the cold pool with divergence behind was also noted as a prominent feature in case studies of these squall lines. The results were similar to those observed by (Tepper, 1950) near Wilmington, Ohio where pressure jumps, temperature falls, wind, and precipitation features were observed with squall lines. Tepper referred to the squall lines as propagating "pressure jump lines".

Fujita further developed the description of the pressure fields present in squall lines. In his synoptic analysis of squall lines in the Central United States, Fujita identified three main features of a pressure field: the pressure surge line, the thunderstorm high, and the wake depression (Fujita, 1955). The pressure surge line marks the leading edge of the thunderstorm and moves in the direction the storm will propagate. The thunderstorm high, which later would be more commonly known as a mesohigh, is the high pressure region led by the pressure surge line and contains cool downdrafts that spread out upon reaching the surface. The region of surface cooling from these downdrafts is what would become known as the cold pool of the

thunderstorm and is often associated with the mesohigh. The wake depression is a region of low pressure, usually behind the thunderstorm high, which forms a pressure dipole with the thunderstorm high.

These pressure dipoles result in a density current forming, marked with a gust front on the leading edge (Wakimoto, 1982). Density currents generally tilts forward with height due to surface drag effects (Markowski and Richardson, 2012). The deeper a density current, the slower the propagation speed, and vice versa (Seigel and van den Heever, 2012). The magnitude of density current speed is roughly the order of magnitude as the downdraft speed since downdrafts can sustain the surface divergence and density current.

Cold pools can have a large range of sizes. Those associated with a single cumulonimbus cell can be on the order of a few km (Tompkins, 2001) while cold pools associated with an mesoscale convective system (MCS) can be on the order of 100-400 km wide (Stensrud et al., 1999). Cold pool depths have a wide range of sizes as well, from around 1 km up to 4 km (Roux, 1988; Weisman and Rotunno, 2005). Estimates of cold pool depth have been made using surface pressure perturbation and virtual temperatures of the cold pool (Stensrud and Fritsch, 1994). The Tompkins study had a mean lifetime of 2.5 hrs while other studies have looked at cold pools that last over 6 hrs (Young and Perugini, 1995).

Based on this early work, a convective cold pool is a region of cold air at the surface in a convectively initiated system. The cooling is a result of evaporative precipitation in the system and can also be influenced by downdrafts; however, downdrafts are not a necessary component. A pressure jump is expected as a result of the hydrostatic adjustment to cooling. Surface divergence is another common feature associated with the pressure gradient resulting in a density current.

For this thesis, cold pool area includes regions of strong surface divergence following temperature decreases and pressure increases. As a result of divergence being the factor turning off a Mesonet triangle from cold pool status, not all areas with precipitation following a frontal passage are included, nor are all areas with a lingering postfrontal temperature decrease. Thusly, cold pool areas and durations in this analysis will generally be smaller and shorter than what would likely be the case

in other studies looking at cold pools. The cold pools defined here can be considered to represent regions of active mesoscale cold air mass production at the surface as a result of precipitation processes. Other parts of a system not defined as a cold pool in this study but likely to be picked up as a cold pool in other studies may be considered to be in a residual cold pool; however, those areas are not explicitly determined in this study.

1.3 Outflow Boundaries

One of the important features of a convective cell are the outflow characteristics. Outflow boundaries can mark the edge of a cold pool as subsiding air reaching the surface spreads out.

Modeling of the updrafts, downdrafts, and outflow of a convective cell is crucial in order to accurately represent the storm evolution. These outflows oftentimes feed back into the convective region of the thunderstorm, allowing the storm to maintain intensity, or form new convective cells as has been found in cloud model simulations (Wilhelmson and Klemp, 1978). Simulations have found that cells can continue to develop for hours at roughly half hour intervals along a progressing outflow boundary (Wilhelmson and Chen, 1982). Their study found that development of modeled and observed cells was generally over or just behind the outflow boundary of previous cells with precipitation-induced downdrafts the primary cause of outflow sustainability.

It has also been found that outflows from multiple clouds can induce lifting, warming, and moistening where they collide (Droegemeier and Wilhelmson, 1985a). In that study, the outflow from two initial convective cells triggered a pair of convective cells to form with the upshear cell continuing to grow. The downdrafts of the upshear cell prevented further development of the downshear cell. A third cell formed from the air lifted over the gust front. A model simulation was run and showed that vertical wind shear strength was the primary factor in determining the growth of the upshear and downshear cells with weaker wind shear allowing for both to grow (Droegemeier and Wilhelmson, 1985b). Further research on thunderstorm outflows examined parameters related to a prescribed horizontal cold air flux in a model simulation (Droegemeier and Wilhelmson, 1987). These parameters are the

vertical temperature profile shape, the magnitude of the temperature deficit, and the outflow depth at the left lateral boundary. The vertical temperature profile shape was the primary controlling factor of the three due to its influence on the gust front speed and outflow depth.

Outflow boundaries can interact with other boundaries such as drylines. A dryline is a sharp surface moisture gradient line at the trailing edge of a continental air mass (Schaefer, 1974). In Great Plains cases, the dryline marks the separation between dry continental air from the west near the elevated terrain of the Rockies and moist tropical air from the Gulf of Mexico. In a case study during the Verification of the Origins of Rotation in Tornadoes Experiment (VORTEX) it was found that a secondary circulation formed above the cold pool (Weiss and Bluestein, 2002). Proposed methods of convective initiation in that particular case were superposition of boundaries and the possibility of the outflow boundary causing parcels to reach their LFC west of the dryline.

1.4 Squall Line and Bow Echo Studies

There has been extensive study of various squall line and bow echo cases throughout the years.

Various studies have looked at the sustainability of squall lines with or without cold pools. One such study found that the interaction of a surface cold pool with low-level wind shear leads to deeper and less inhibited lifting which allows for new cells to form more easily (Rotunno et al., 1988). However, it has also been found that a squall line can sustain itself without a cold pool present, as was the case in a case study using the fifth-generation Pennsylvania State University-NCAR Mesoscale Model (MM5) (Stoelinga et al., 2003). In the case without a cold pool, a cold front aloft provided the main source of lifting to sustain the squall line. Due to the variety of squall line cases and the frequent lack of clear indication of whether or not a system is a squall line, these results are possibilities rather than rules.

A cloud-resolving model at high-resolution has been used to study tropical-deep-convection-generated cold pools (Tompkins, 2001). Tompkins had found an average lifetime of 2.5 hrs, with lifetime based on the duration in which all the points lying

within a radius of the center point of a cold pools is less than the threshold buoyancy of -0.005 m^2s^{-1} and an average maximum radius of 8.6 km. From the study a three-stage model was developed. Stage one involves cooling and moistening through evaporated precipitation below the area of convection before the downdraft develops. Stage two involves the spreading of a boundary layer cold pool. The final stage involves the entrainment of elevated air into the weakening downdraft. This study also found that cold pools are initiated in low wind shear cases predominantly due to the thermodynamical cause of higher cold pool water vapor and equivalent potential temperature values in the environment surrounding the outer regions of the wake.

Observational case studies are common in the Great Plains region of the United States, particularly during Intensive Observation Periods (IOPs) when extra equipment is available in field campaigns. Sounding data allowed a squall line in the Second Verification of the Origins of Rotation in Tornadoes Experiment (VORTEX2) to be observed in great detail (Bryan and Parker, 2010). The cold pool depth of 4.7 km reached above the melting layer suggesting that sublimation was a factor in this case.

Cold pool features accompany bow echoes as well. Bow echoes are bowing segments of intense convection with rear inflow directed at the center of the bow behind the gust front (Weisman, 2001). Using model simulations of bow echoes it was found that long-lived segments develop most favorably with intermediate values of water vapor concentrations resulting in a local portion of the cold pool overwhelming low-level shear (James et al., 2006). They found that cold pools that were dry in the middle-troposphere tended to lose heterogeneity in structure with the convection becoming upshear tilted everywhere before a bow can develop in the line.

1.5 MCS Studies

Many observational studies of mesoscale convective systems (MCSs) have allowed for analysis of cold pools.

Pressure features and precipitation structure have been detailed in Oklahoma-Kansas Preliminary Regional Experiment for STORM-Central (OK PRE-STORM) cases of MCSs (Stumpf et al., 1991; Loehrer and Johnson, 1995). The primary finding in Stumpf et al. was that trailing stratiform regions of MCSs resulted in warming of

the lower troposphere, strong low-level winds, and a pressure gradient associated with a wake low. The Loehrer and Johnson study found that, despite a large variety in inital structure of precipitation, storms tended to develop, through varying paths, to an asymmetrical pattern with leading convective lines with stronger cells to the south and trailing stratiform precipitation prominent in the left rear flank. Their conceptual model of the symmetrical and asymmetrical patterns suggests the cold pool in asymmetrical stages of the MCS life cycle would be displaced towards the left rear flank.

Pressure transients, comprising of mesohighs and wake lows, were observed in Preliminary Regional Experiment for Storm-Scale Operational Research Meteorology (PRE-STORM) MCSs (Knievel and Johnson, 1998). The transients were roughly 100 km apart, had a magnitude of a few mb, and lasted an average of 2 hrs. Pressure gradients increased in magnitude as an MCS matured while the size and number of transients were related to stratiform and convective rain rates.

Flow relative to cold pools and the conditional instability distribution along gust fronts were shown to be a primary determinant on the propagation direction of an MCS (Corfidi, 2003). Corfidi found that for many MCSs this direction coincides with the direction of the low-level jet; however, for bow-echo systems where the system may move faster than the mean wind, the downwind vector is more representative of their motion.

Cold pools are important to have represented accurately in severe weather forecasting. In one particular modeling case study, the model success was highly dependent on having a reasonably accurate initialization of low-level flow patterns allowing for improvements in model predictions of later cells (Romero et al., 2001).

1.6 Parameterization Studies

1.6.1 Shallow and Deep Convection

Parameterizations of deep convection have been proposed over the years with the mass flux scheme commonly used (Arakawa and Schubert, 1974). Arakawa and Schubert's method involves parameterizing cumulus convection through the use of vertical distribution of mass flux, the entrainment and detrainment rates, and

thermodynamic properties. Their cloud work function measures the buoyancy force in clouds and allows for a closed parameterization of cumulus convection.

With schemes developed for shallow convection and deep convection, a necessary task undertaken in recent years is to develop a bridge to span between the two. One approach is through the use of precipitation evaporation (Hohenegger and Bretherton, 2011). Cloud-base mass flux, cloud-base humidity, and entrainment and detrainment rates were adjusted in the University of Washington shallow convection scheme to improve simulation of deep convection. A convective inhibition/turbulent kinetic energy (CIN/TKE) closure scheme maintained cloud base near the planetary boundary layer (PBL) top while increases in cloud-base mass flux as a result of cold pool effects alter the height of the PBL, affecting convective development.

1.6.2 Rain Evaporation and Downdrafts

An early attempt to parameterize variables related to cold pools involved development of a method for estimating the relationship between rain evaporation in a convective system to the hydrostatic surface pressure anomaly in a cold pool (Fujita, 1959). It was found that the increased cold air mass and the evaporated rain had a quantitative relationship dependent on the temperature lapse rate below cloud base. As a result, pressure changes at the surface in connection in cold pools can lead to estimates of rain evaporation.

A study of National Centers for Environmental Prediction (NCEP) mesoscale Eta model forecasts was performed (Stensrud et al., 1999) which parameterized 1) convection, 2) planetary boundary layer and surface physics, 3) explicit microphysics, and 4) initialization and data assimilation. It was found that the model was significantly influenced by cold pools for the case where the large scale forcing was rather weak, and weakly influenced by cold pools for cases where the large scale forcing was strong. The study notes that this result was largely due to the lack of convective downdraft effects in the convective parameterization scheme selected.

Rain evaporation has been incorporated into downdraft parameterizations for use with cumulus updraft schemes (Sud and Walker, 1993). When tested on GATE [GARP (Global Atmospheric Research Program) Atlantic Tropical Experiment] data the rain evaporation and downdraft parameterization improved tropospheric temper-

ature simulation results for surface temperatures and precipitation.

Variability of droplet size distributions hinders the capabilities of the parameterization of rain evaporation (Seifert, 2008). However, bulk microphysics schemes for multimoment models have been developed to enhance evaluation of the microphysics involved in cold pools (Dawson et al., 2010). Several advantages of this scheme were improved representation of rain evaporation, drop size distributions, and reduction of the cold bias in convective storm downdrafts and associated cold pools found in single-moment schemes.

1.6.3 General Circulation Model (GCM) Parameterizations

Parameterization schemes were developed for the surface outflow regions of cold pool (wake) downdrafts where new convection is triggered at the edges (Qian et al., 1998). Wake recovery times were on the order of hours as was observed during GATE and the Tropical Ocean and Global Atmosphere Coupled Ocean-Atmosphere Response Experiment (TOGA COARE).

Available lifting energy (ALE) and available lifting power (ALP) were used in the ALE/ALP closure method created to represent the coupling between the convection and the cold pool (Grandpeix and Lafore, 2010). This closure scheme was able to more realistically represent moist convective processes and to simulate cases in a 1D single column model with results close to the observations and cloud resolving model (CRM) simulations (Grandpeix et al., 2010). The depth of the wake for the continental case was twice as much as for the oceanic case. In addition, the temperature drops were twice as strong for the continental case. ALP closure parameterizations have been used more recently in 3D configuration of the LMDZ5B GCM after adjusting the vertical velocity for the environmental conditions in which the wake resides (Rio et al., 2012). The ALP closure altered the precipitation patterns seasonally and diurnally in the model, notably the late afternoon peak in continental precipitation which corrected a bias common in GCMs.

The rest of this thesis is organized as follows. The description of the Oklahoma Mesonet and precipitation datasets are detailed in Chapter 2. Mass flux, precipitation, frontal passage, and cold pool methodology is outlined in Chapter 3. Results for mass flux and precipitation data are covered in Chapter 4. Several case studies

during the 15-yr study period are detailed in Chapter 5. Fifteen year front and cold pool climatologies are detailed in Chapter 6. These climatologies include the changes in key variables during frontal passages, the convergence/divergence associated with frontal passages, and the seasonal, diurnal, and geographic distribution of frontal passages and cold pools. The discussion of the results is located in Chapter 7. The conclusions and future work make up Chapter 8.

CHAPTER 2

DATA

2.1 Oklahoma Mesonet

The Department of Energy Atmospheric Radiation Measurement (ARM) Program's Oklahoma Mesonet is the primary dataset used in this research (Brock et al., 1995; McPherson et al., 2007). The Oklahoma Mesonet is sponsored by the University of Oklahoma and Oklahoma State University. Data from the Mesonet have been collected since 1994 at a 5-min frequency. Over 100 stations are distributed roughly 40 km apart with at least one station in each county of Oklahoma.

Stations have been added over the years but for the purposes of this study, only the initial 114 stations that were present in 1997 are considered. Six of these stations are located in the Oklahoma Panhandle and are excluded. For the remaining stations, each station is used in this study only for the years in which the focus variables all exceed the observation threshold of 90% of annual measurement times having data recorded. The focus variables used in this study are longitude, latitude, altitude, 1.5-m air temperature, 1.5-m relative humidity, 10-m vector average wind magnitude, 10-m vector average wind direction, station pressure, and surface precipitation. Longitude and latitude only change in the case of a few stations which changed location over the 15-yr period (1997-2011). Those stations were excluded the year that they moved. Each year had between 99 and 104 of the 108 nonpanhandle stations meet the observation threshold.

Mesonet stations that met the observation threshold for a year were gridded using the Delaunay triangulation procedure (Fig. 2.1). The resulting grid contains some extremely narrow triangles along the border which have been removed. Two stations very close to each other located near 35N 98W resulted in two small, narrow triangles that have also been removed.

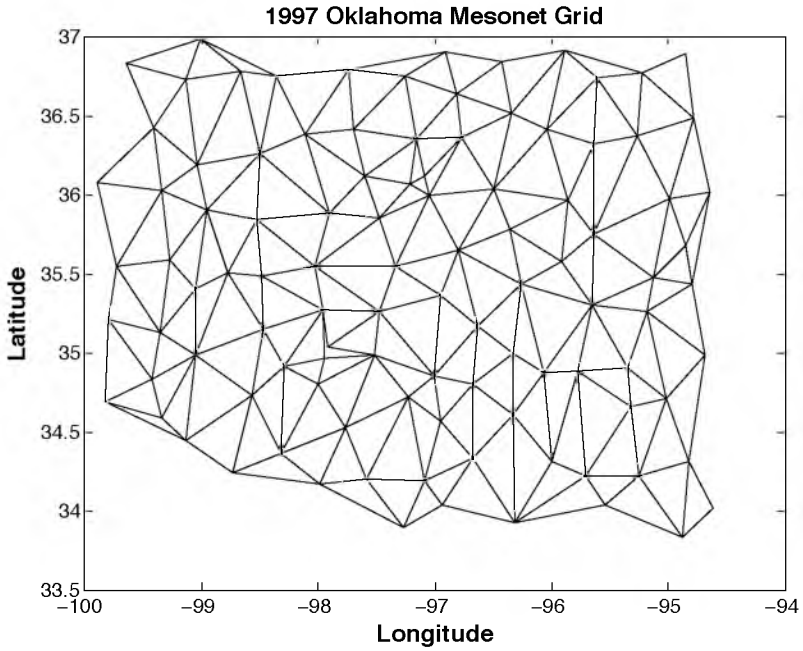

Figure 2.1 – Map of the Oklahoma Mesonet grid used for 1997. Delaunay triangulation was used to plot the stations onto the grid and particularly long and skinny triangles were removed. Removed triangles were primarily on the outer border with the exception of two near 98W and 35N.

In the process of this study it was determined that triangles with too long a side length were not representative so any triangle with a maximum side length of at least 80 km was excluded. This resulted in the removal of 10-13 triangles each year. Due to the varying number of stations that met the observation threshold each year, the grid is adjusted slightly from year to year.

2.2 Arkansas-Red Basin River Forecast Center Gridded Precipitation

A 4-km x 4-km gridded precipitation dataset produced by the Arkansas-Red Basin River Forecast Center (ABRFC) was used in this study to compare to the Oklahoma Mesonet precipitation values. The ABRFC gridded precipitation values are a result of a combination of Weather Surveillance Radar 88 Doppler (WSR-88D) Next-Generation Radar (NEXRAD) (Crum et al., 1993, 1998) precipitation estimates and rain gauge reports (Fulton et al., 1998). The inclusion of rain gauge reports to help reduce radar estimate biases has made the gridded precipitation values reliable

at monthly and daily timescales (Grassotti et al., 2003). These gridded precipitation estimates are available from 24 June 1994 though only the period from May-August 1997 was used in this study for the purposes of determining whether or not the Mesonet precipitation values are representative of the Oklahoma Mesonet domain.

CHAPTER 3

METHODOLOGY

Using Mesonet surface observations divergence values can be calculated. These divergences can be used as a proxy to identify near-surface mass fluxes as detailed in section 3.1. Precipitation can be related to these estimates; however, the Mesonet precipitation values need to be compared to other data to determine representativeness. This representativeness check is detailed in section 3.2. The process of identifying frontal passages and cold pools follows in sections 3.3-3.4.

3.1 Mass Flux Estimates

Having identified the grid for the Mesonet domain to be used in this study, the wind speed and direction values from the Mesonet dataset are used to determine the divergence in each Mesonet triangle. Equations 3.1-3.4 identify a set of determinants which were used to calculate the horizontal divergence of triangles that are part of an irregular grid and has previously been applied to mesonet datasets (Davies-Jones, 1993; Dubois and Spencer, 2005).

$$a = \frac{\det \begin{pmatrix} u_2 - u_1 & y_2 - y_1 \\ u_3 - u_1 & y_3 - y_1 \end{pmatrix}}{2A(0)} \tag{3.1}$$

$$d = \frac{\det \begin{pmatrix} x_2 - x_1 & v_2 - v_1 \\ x_3 - x_1 & v_3 - v_1 \end{pmatrix}}{2A(0)} \tag{3.2}$$

$$A(0) = \frac{\det \begin{pmatrix} x_2 - x_1 & y_2 - y_1 \\ x_3 - x_1 & y_3 - y_1 \end{pmatrix}}{2} \tag{3.3}$$

$$D = a + d \tag{3.4}$$

The procedure from Sun and Krueger (2012) was used to estimate the updraft and downdraft mass fluxes using estimates of surface divergence averaged over the Mesonet domain. Sun and Krueger's equations for boundary layer updraft, M_u (Eq. 3.5), and downdraft, M_d (Eq. 3.6), mass fluxes are

$$M_u = \frac{-\sum_i (A_i) D_i H(-D_i))}{\sum_i A_i} \tag{3.5}$$

$$M_d = \frac{\sum_i (A_i) D_i H(D_i))}{\sum_i A_i} \tag{3.6}$$

where D_i is the horizontal divergence of the ith triangle, A_i is the area of the ith triangle, and $H(D_i)$ is the Heaviside step function. Additionally, regions of strong convergence and divergence are identified to better identify likely regions of precipitation. M_u^+ and M_d^+ are identified as were M_u and M_d except the Heaviside step function only accepts regions of convergence or divergence that exceed a magnitude $> 10^{-4}\text{s}^{-1}$ (Eq. 3.7-3.8).

$$M_u^+ = \frac{-\sum_i (A_i) D_i H(-D_i > 10^{-4}\text{s}^{-1}))}{\sum_i A_i} \tag{3.7}$$

$$M_d^+ = \frac{\sum_i (A_i) D_i H(D_i > 10^{-4}\text{s}^{-1}))}{\sum_i A_i} \tag{3.8}$$

3.2 Precipitation

Mesonet precipitation values were determined through an area-average over the entire Mesonet domain. The area-averaging was calculated by attributing each station precipitation observation to 1/3 of the area of each triangle in which the station was a corner. Since the Mesonet precipitation estimate over the domain uses only ~100 points, a comparison with the ABRFC gridded precipitation values was performed to check the representativeness of the Mesonet precipitation data.

The ABRFC grid is defined as an average of all the points with longitudinal boundaries of 100.0W and 94.5W as well as latitudinal boundaries of 33.8N and 37.0N. A corner of the boundary that is entirely outside of Oklahoma is left out as well, stretching from 33.8N 97.6W to 34.6N 100.0W with points to the southwest dropped while points northeast were retained in the comparison. The ABRFC domain is the region marked in magenta (Fig. 3.1a).

Hourly precipitation totals for the Oklahoma Mesonet and ABRFC datasets were generated for the May-August 1997 period. The correlation between the four months of hourly estimates of Mesonet precipitation, using these two methods, was 0.95. The strong correlation suggests that filling in the gaps in triangles using interpolation of the Mesonet station values is capable of adequately representing the precipitation totals derived from the ABRFC radar estimates. A case comparison of the two datasets for a 1-hr period from 7-8 UTC 2 May 1997 shows a strong likeness (Fig. 3.1).

3.3 Front Analysis

Identifying frontal passages in the Oklahoma Mesonet is necessary to identify cold pools. However, not all frontal passages have an associated cold pool. Cold pools are marked on the leading edge by a gust front. Previous studies have shown that temperature falls and pressure rises are associated with cold pools and these gust fronts (Engerer et al., 2008; Adams-Selin and Johnson, 2010).

The frontal passages analyzed, as will be described in this section, mark the cold front where the temperature drop occurs. The forward edge of the cold pools analyzed, as will be described in section 3.4, mark the gust front which is the leading edge of surface divergence. Frequently the cold front and gust front are co-located.

In addition to fronts associated with convective and mesoscale systems, synoptic fronts can also be picked up in the front analysis since temperature falls and pressure rises are the identifiers for frontal passages in this study.

Temperature and pressure values at each station were adjusted to remove the signal of the diurnal cycle. The diurnal cycle was calculated by averaging the valid observations at a station during the 15-yr period at the same timestep (0000 UTC, 0005 UTC,...,2355 UTC) and then using 5-day averages centered on the day (Eq. 3.9) where n is the total number of valid observations summed and t is the current 5-min

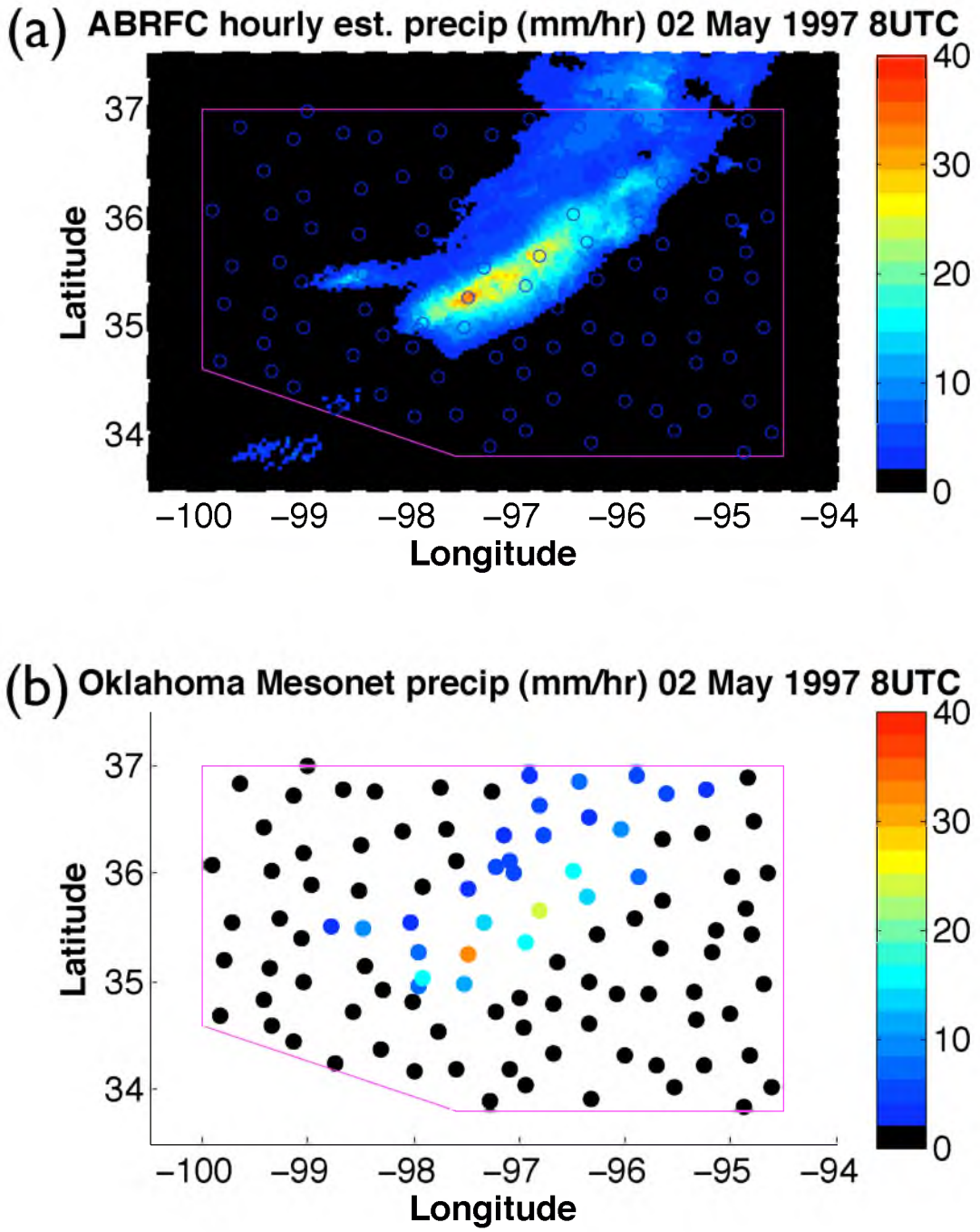

Figure 3.1 – Hourly precipitation total ending at 8 UTC on 2 May 1997 in mm/hr from (a) ABRFC radar estimated precipitation and (b) Oklahoma Mesonet precipitation observations. The box indicates the area used to determine the ABRFC total Mesonet precipitation estimate. Only the area inside the triangles is considered for the Oklahoma Mesonet total precipitation estimate.

timestep. For example, 12 June 0000 UTCs diurnal value at a station would be the average of all 0000 UTC observations at that station from 10-14 June for the 15-yr dataset. Without the removal of the diurnal cycle many spurious frontal passages are generated in the analysis in the late afternoon hours as the sun is setting. Similarly, the diurnal cycle was also calculated for the pressure observations (Eq. 3.10).

$$T_{\text{diur.}} = [\sum_{1997}^{2011} \sum_{\text{day}-2}^{\text{day}+2} T_t]/n \tag{3.9}$$

$$P_{\text{diur.}} = [\sum_{1997}^{2011} \sum_{\text{day}-2}^{\text{day}+2} P_t]/n \tag{3.10}$$

Pressure and temperature values at each station were also adjusted to account for the differences in elevation. Each station was adjusted to the Mesonet-averaged elevation, between 365 and 370 m depending on year since only stations which met the observation threshold in a particular year were included in the average altitude for that year.

For pressure, the elevation adjustment involved several steps based in part on equations (3.11-3.14 below) from Wallace and Hobbs (2006). Using temperature before diurnal adjustments were made, the saturation vapor pressure, e_s, is calculated (Eq. 3.11). Using saturation vapor pressure and relative humidity (RH), the vapor pressure (e), water vapor mixing ratio (q_v), virtual temperature (T_v), and then finally elevation adjusted pressure changes are calculated (Eq. 3.12-3.15). $T_0 = 273.15$ K while z_{station} and z_{mean} are the altitudes of the Mesonet station and the mean of the Mesonet station altitudes. Since the diurnal and elevation changes are desired, the change in pressure with the elevation adjustment only is applied to the diurnal adjusted temperature (Eq. 3.16). The temperatures used in the equations for e_s and T_v, however, are the observed temperatures before diurnal adjustment.

$$e_s = 6.11 \exp(5420(\frac{1}{T_0} - \frac{1}{T})) \tag{3.11}$$

$$e = e_s \frac{RH}{100} \tag{3.12}$$

$$q_v = \frac{.622e}{P - e} \tag{3.13}$$

$$T_v = T(1 + .61q_v) \tag{3.14}$$

$$P_{\text{elev.}} = P \exp(\frac{z_{\text{station}} - z_{\text{mean}}}{29.3T_v}) \tag{3.15}$$

$$P_{\text{diur.,elev.}} = P_{\text{diur.}} - (P - P_{\text{elev.}}) \tag{3.16}$$

For temperature, the elevation adjustment was calculated by lifting or descent the station value dry adiabatically to the average elevation (Eq. 3.17).

$$T_{\text{diur.,elev.}} = T_{\text{diur.}} + 9.8(z_{\text{mean}} - z_{\text{station}})/1000 \tag{3.17}$$

Additionally, the change in moist static energy (Δhc_p^{-1}) was calculated in temperature units (K) using the elevation adjusted temperatures and water vapor mixing ratio (Eq. 3.18).

$$\Delta hc_p^{-1} = T_{\text{final,diur.,elev.}} - T_{\text{initial,diur.,elev.}} + (Lc_p^{-1})(q_{v,\text{final}} - q_{v,\text{initial}}) \tag{3.18}$$

L is the latent heat of evaporation, 2.5×10^6 Jkg^{-1}, and c_p is the specific heat of dry air at constant pressure, 1004 Jkg^{-1}K^{-1}.

The front score (FS) is a unitless variable used in this study to represent the strength of a frontal passage. The FS incorporates diurnal and elevation adjusted pressure rises and temperature falls over 30-min intervals, calculated every 5 mins, so that the front score at 1230 UTC compares station temperature and pressure at 1230 UTC to the station temperature and pressure at 1200 UTC. A 1 mb pressure increase is considered the equivalent of 1 K of temperature fall. Adding these differences

yields the front score (Eq. 3.19). An example of FSs at a station over several months is shown for JJA 1997 at the Blackwell Mesonet station (Fig. 3.2).

$$FS_{\text{final}} = 1\,\text{mb}^{-1}\Delta P_{\text{diur.,elev.}} - 1\,\text{K}^{-1}\Delta T_{\text{diur.,elev.}} \tag{3.19}$$

FSs are used to determine whether or not a frontal passage occurs at a station or Mesonet triangle. A front is considered to have reached a Mesonet station when the FS at a station exceeds a minimum threshold. Also, the FS at the station must be the highest it reaches within 3 hrs in either direction in order to identify the primary front associated with a system. FSs of 3 and 5 are used as thresholds for fronts and strong fronts, respectively. The 30-min period generating the highest FS value for a front is, in the vast majority of cases, also the first 30-min period with a FS exceeding the threshold value.

A frontal passage at a Mesonet triangle (in contrast to one at a Mesonet station) is determined to have occurred if all three stations that comprise the corners of the triangle experience a frontal passage within a 2-hr span. The 2-hr limit is the reason that maximum triangle side length was limited to 80 km since slower fronts are less likely to be detected in larger triangles leading to an underestimate in front frequency. However, if the 2-hr limit had been extended more spurious fronts would have been captured. This limit was chosen in an effort to minimize the number of spurious fronts detected and the number of legitimate fronts missed. The duration of the frontal passage at a triangle is from the time the first corner is reached by the front to the time the third corner is reached by the front. These fronts are assumed, due to lack of additional stations in the middle of the triangle, to have advanced at a constant speed as they progress through the Mesonet triangle. Additionally, these fronts can be tracked across the Mesonet as they progress in various case studies, detailed in Chapter 5.

3.4 Cold Pool Analysis

The front analysis is necessary for determining the location of potential cold pools since gust fronts mark the leading edge of cold pools (Wakimoto, 1982). Cold

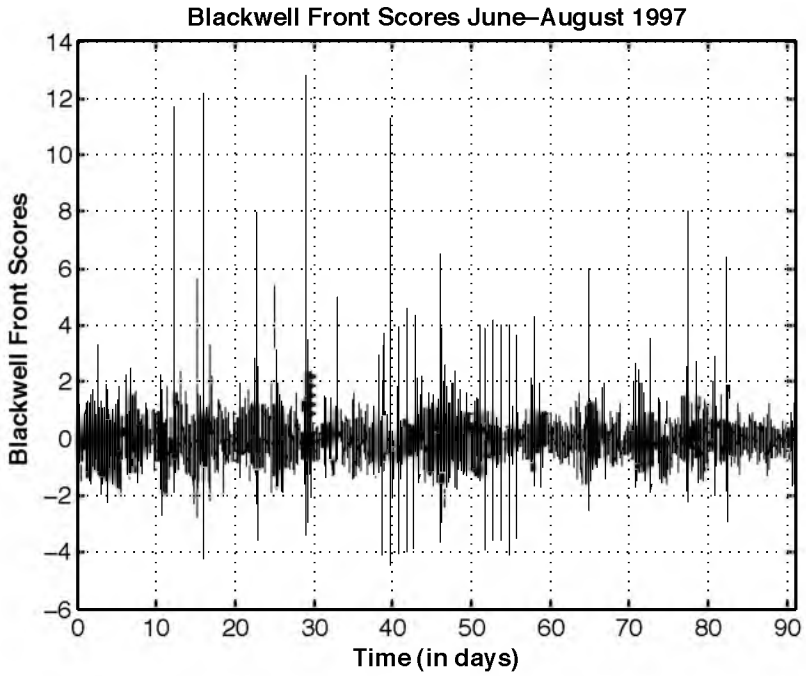

Figure 3.2 – Front scores for the JJA 1997 period at the Blackwell Mesonet station (36.75N, 97.25W). High, positive front scores indicate frontal passages.

pools are primarily identified with temperature falls and pressure rises, much like the frontal passages themselves. Additionally, active cold pools are regions of surface divergence, which is the additional identifier used in this study to isolate fronts associated with active cold pools from the rest of the frontal passages. As a result, the cold pool boundaries are defined in this study by Mesonet triangles of surface divergence following a temperature drop and pressure rise. This definition is more limiting than that used by other studies where continuing precipitation or a lack of surface temperature recovery indicates a sustained cold pool. The cold pools in the following Oklahoma Mesonet analysis are representative of the regions where a cold air mass is expanding or building via precipitation processes whereas the areas that would be considered a cold pool in other studies but not this study are areas of cold air maintenance due to a lack of surface heating.

A cold pool is determined to have been detected at a Mesonet triangle if the triangle experiences a frontal passage and if the 15-min averaged strong divergence threshold ($D_i > 10^{-4}\text{s}^{-1}$) is met within half an hr before or an hr after the frontal

passage reaches the timestep that is halfway between its progression through the triangle. The longer time duration after the frontal passage is due to cold pools being behind gust fronts. It is possible, given the resolution of the Mesonet grid, that a cold pool could seemingly be in place ahead of a front. This would be a circumstance where the 15-min divergence average for a Mesonet triangle meets the strong divergence threshold slightly before the front reaches halfway across the Mesonet triangle and would indicate a strong cold pool covering less than half of the triangle. Given the limitations in the resolution of the Mesonet grid, however, the possibility of a cold pool being present just before the front reaches the middle of the triangle is considered plausible.

When a cold pool is determined to have occurred for the given frontal passage the duration of the cold pool is calculated. This is done by finding the divergence maximum and moving in both directions through time from the timestep of the divergence maximum until the divergence falls below half the maximum divergence value for that triangle.

Dry frontal passages generally did not result in cold pools in the cold pool analysis due to insufficiently high divergence values. However, this is not the case for all dry frontal passages as there were some exceptions. These fronts were generally synoptic in nature, due to low surface divergence and a lack of evaporative precipitation.

Case studies are looked at using radar composite images from the National Center for Atmospheric Research (NCAR) image archive for the southern plains in Chapter 5. Statistics can be calculated for the fronts and cold pools identified by these methods and are detailed in Chapter 6.

CHAPTER 4

RESULTS: MASS FLUXES AND PRECIPITATION

4.1 Mass Fluxes

As detailed in Chapter 3, for the 15-yr dataset the updraft and downdraft mass flux estimates M_u, M_d, M_u^+, and M_d^+ were calculated as averages over the entire Mesonet domain. Monthly averages were computed and an annual cycle can be observed. In the spring months the magnitude of the variables are, more often than not, larger in magnitude than the other seasons (Fig. 4.1).

The annual cycles for M_u, M_d, M_u^+, and M_d^+ were calculated with the means and ranges (Fig. 4.2). For each of the four variables the divergence or convergence magnitude is largest in the spring. The magnitudes are lowest in September for the updraft variables and around November/December for downdrafts. For M_u and M_d the difference between the highest and lowest monthly averages is approximately 10%. For M_u^+ and M_d^+ the differences are approximately 20%. The seasonal cycle is strong enough that there is at least one month for each variable for which all 15 yrs of values for that month were below the average of another month, and a month for which all 15 values were above the average of another month. For example, in Fig. 4.2a the lowest April value was higher than the mean value of all months from July through February, while all November values were lower than the mean values for March through June.

4.2 Precipitation

Precipitation values were also calculated for the 15-yr Mesonet dataset (Fig. 4.3). June 2007 was the wettest month at 8.56 mm/day. No other month exceeded 7 mm/day. The driest months were January 2003 and August 2000 with values of .061

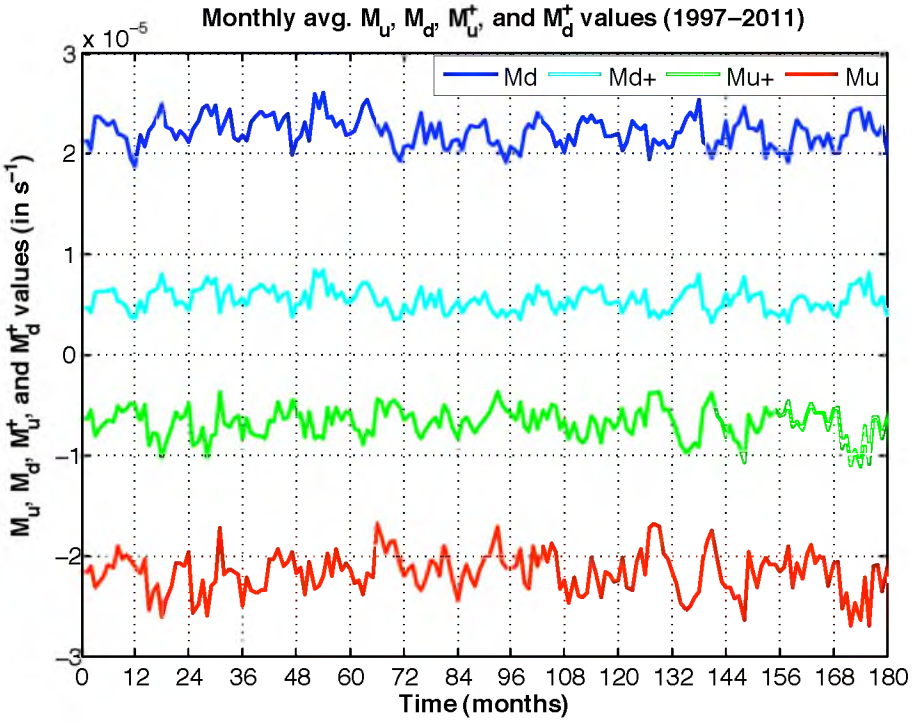

Figure 4.1 – Oklahoma Mesonet monthly values for M_u (red), M_d (blue), M_u^+ (green), and M_d^+ (cyan) over the 1997-2011 period. These values are averaged over the entire Mesonet area. Since stronger divergence/convergence is a subset of all convergence/divergence M_u^+ and M_d^+ are greater in magnitude than M_u and M_d.

mm/day and .072 mm/day respectively (Fig. 4.3a). June and May are the wettest months on average, while December and January are the driest on average (Fig. 4.3b). Despite the annual cycle, each month had a year with less than 1.5 mm/day of rain and a year with more than 3 mm/day which is a result of the large variability from year to year in Fig. 4.3a.

Correlations were then calculated between the 3-hr averaged convergence/divergence and Mesonet precipitation variables for the 15-yr period (Table 4.1). Correlations between surface convergence and divergence were higher in the summer (JJA, 0.53) than in the other seasons (0.31, 0.28, 0.24). Likewise, correlations between strong convergence and strong divergence were higher in the summer (JJA, 0.78) than the other seasons (0.69, 0.67, 0.65) though the magnitude of the correlation difference is smaller. Convergence and divergence had higher correlations with Mesonet precipi-

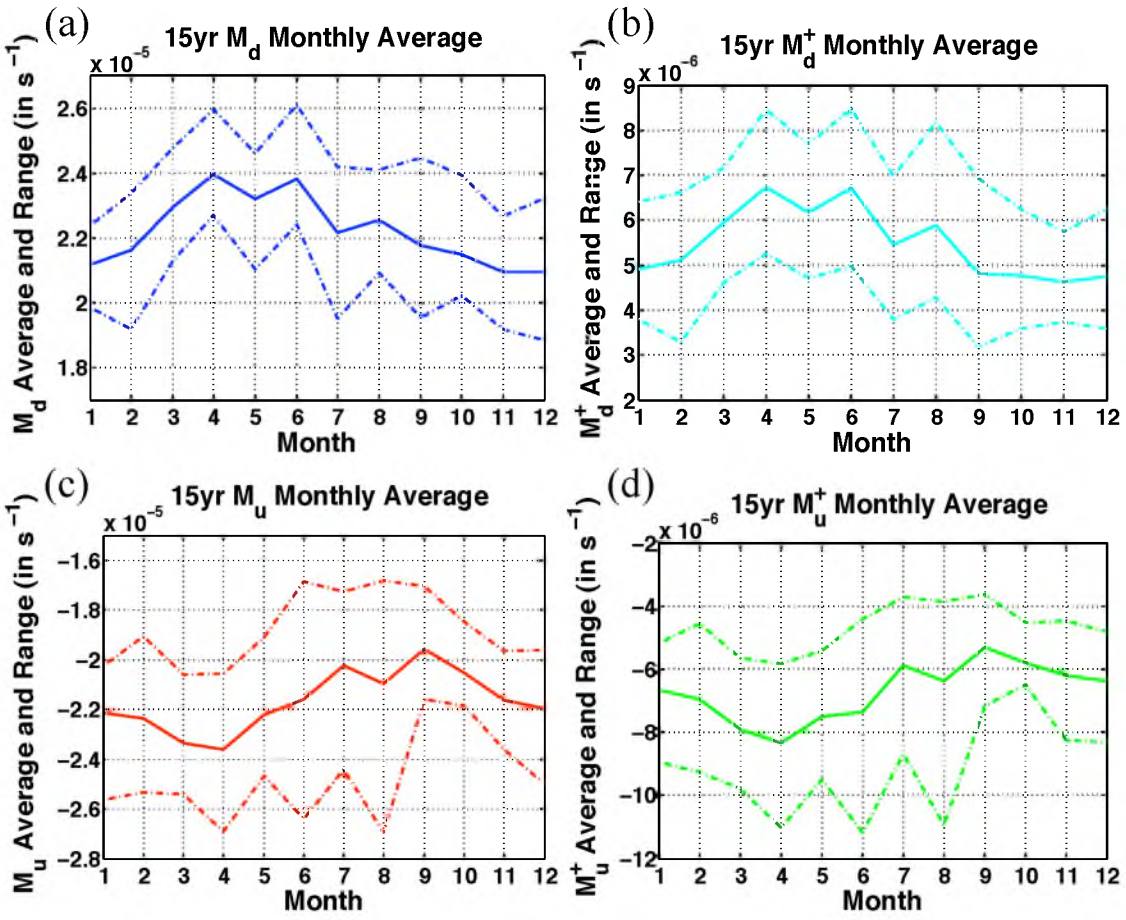

Figure 4.2 – Annual cycle of (a) M_d, (b) M_d^+, (c) M_u, and (d) M_u^+ values for the Oklahoma Mesonet with the average and range plotted. Divergence and convergence are stronger on average in spring than the other seasons while convergence is weakest in September and divergence weakest in November/December.

tation during the spring and summer and had the lowest correlations in the winter. The seasonal disparity is likely influenced by the seasonal pattern of convective vs stratiform precipitation. Convective precipitation is more common in spring and summer while stratiform precipitation is more common in winter. M_u^+ and M_d^+ have higher correlations with precipitation than do M_u and M_d. Since convective precipitation is associated with higher magnitude updrafts and downdrafts on average, this result further suggests an influence of convection where convective precipitation events have stronger correlations between mass fluxes and precipitation than does stratiform precipitation events on average.

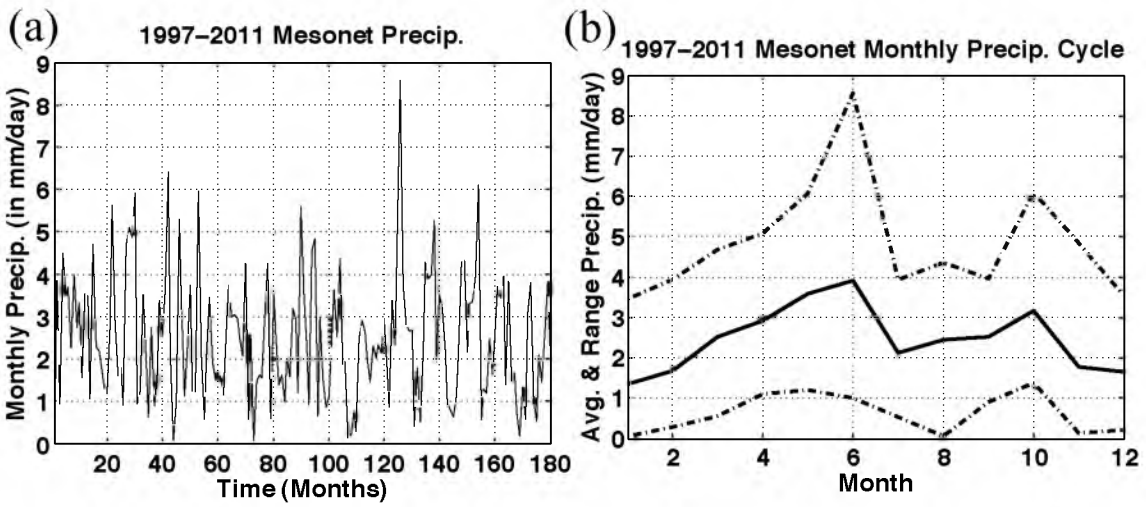

Figure 4.3 – Oklahoma Mesonet (a) monthly average precipitation values over the 1997-2011 period and (b) the monthly averages and range of the annual cycle of precipitation.

Table 4.1 – Correlation table for each of the 4 seasons using the 15-yrs of Mesonet observations for M_u, M_d, M_u^+, M_d^+, and precipitation ($Prec$).

Correlation	$M_u M_d$	$M_u^+ M_d^+$	$M_u Prec$	$M_d Prec$	$M_u^+ Prec$	$M_d^+ Prec$
Spring	0.31	0.69	0.43	0.42	0.49	0.55
Summer	0.53	0.78	0.48	0.48	0.55	0.59
Fall	0.28	0.67	0.40	0.31	0.46	0.44
Winter	0.24	0.65	0.26	0.17	0.31	0.27
Annual	0.35	0.70	0.40	0.37	0.46	0.49

Average surface convergence and divergence for dry and wet days for each season were determined. Dry days are defined as days with 0 mm of precipitation averaged over the Mesonet. Wet days are defined as days with at least 1 mm of precipitation averaged over the Mesonet. This leaves days with 0.01-0.99 mm of precipitation out which allows for more clarity between the two groups. Results show that wet days have stronger convergence than dry days, as expected (Fig. 4.4).

Wet days in the spring and summer had the highest average convergence and divergence. Additionally, summer dry days had the lowest average convergence and divergence giving summer the largest disparity between wet and dry day averages. Winter had the lowest disparity between wet and dry day updraft and downdraft

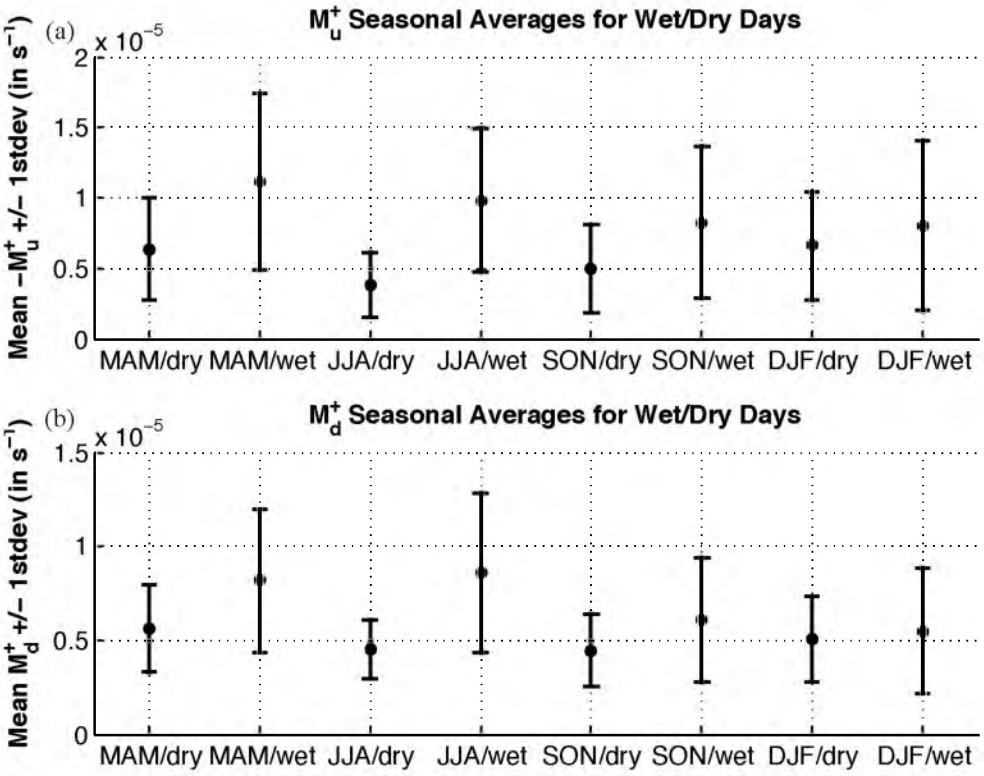

Figure 4.4 – Seasonal average and 1 stdev. for (a) M_u^+ and (b) M_d^+ for wet (Mesonet area averaged precip. > 1 mm) and dry (0 precip.) days. Wet spring and summer days have the strongest average convergence and divergence while dry summer days have the weakest.

averages. Standard deviations were larger for wet days than dry days. This is largely a result of wet days including everything from showers to intense squall lines.

CHAPTER 5

RESULTS: CASE STUDIES

Over 15 yrs of Mesonet data, tens of thousands of frontal passages at triangles were detected in the Oklahoma Mesonet with up to dozens of triangles reached with each front leaving hundreds of events that can be used for case studies. Four such cases will be shown in this chapter: 1) 13 June 1997, 2) 15-16 June 2002, 3) 20 May 2011, and 4) 24-25 May 2011. These cases are supplemented with radar images from the UCAR image archive.

5.1 13 June 1997 Case

Around 0 UTC on 13 June 1997 a squall line, which initiated in southeastern Colorado and northeastern New Mexico, was entering Kansas, the Oklahoma panhandle, and Texas. The disorganized line of thunderstorms entered the Mesonet grid at roughly 3 UTC and was tracked for the next 7 hrs across the Mesonet (Fig. 5.1) with isolated thunderstorms popping up ahead of the main line. At 0330 UTC (Fig. 5.1a) the front analysis found only smaller segments of a front (yellow and magenta segments for fronts and strong fronts, respectively) in the northwest and center-west portions of Oklahoma. The radar images show a gap between two thunderstorms that coincides with the lack of strong convection (gap in the red dots in Fig. 5.1a). In the areas where a front was defined, convergence was present to the east ahead of the front and divergence to the west behind the front. Cold pools were able to be tracked as well (Fig. 5.2) though at 0330 UTC (Fig. 5.2a) there was only one triangle designated as in a cold pool, in the northwestern corner of the Mesonet domain.

From the 5 UTC front analysis (Fig. 5.1b), the stronger, more well-defined front marks the leading edge of the system which had been organizing over the previous

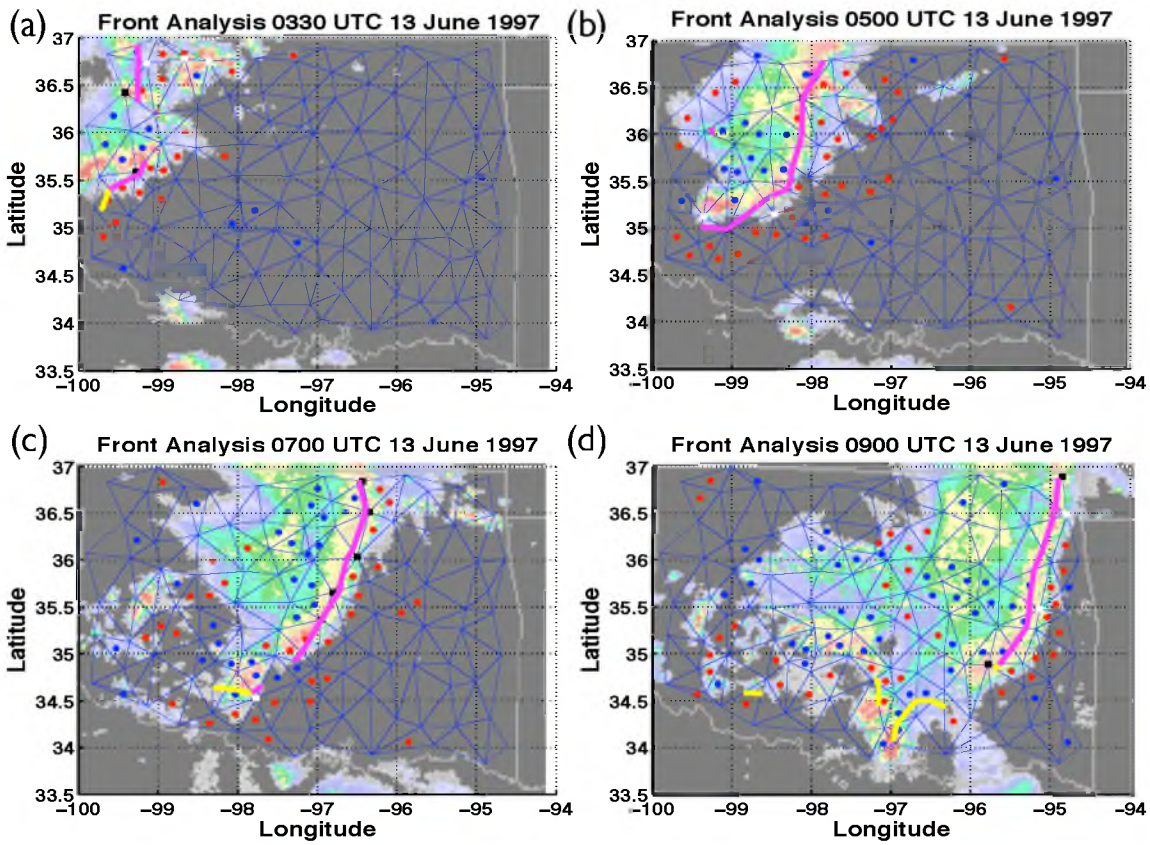

Figure 5.1 – Front analysis for 13 June 1997 (a) 0300 UTC, (b) 0500 UTC, (c) 0700 UTC, and (d) 0900 UTC. Red dots are $D_i < -10^{-4}\text{s}^{-1}$ while blue dots are $D_i > 10^{-4}\text{s}^{-1}$. Yellow lines are frontal passages with FSs of 3 <= FS < 5 while magenta lines are frontal passages with FSs of 5+. White squares are stations where at the current timestep the FS is 3 <= FS < 5; black squares designate stations currently with FSs at 5+. Radar images are from the UCAR image archive.

two hours. There was some bowing of the front present with trailing stratiform precipitation. The squall line had caught up to the isolated thunderstorms that developed ahead of the line. The area ahead of the front had strong convergence while strong divergence was present behind the front. Farther behind the front, near the back edge of the stratiform precipitation, there was a second region of convergence where a one-triangle front is marked. The analysis was designed to capture the strongest fronts at each triangle and in this case this latter front was stronger than when the initial line passed through heading eastward. This was likely a result of the squall line being somewhat disorganized in that area at the time it passed that

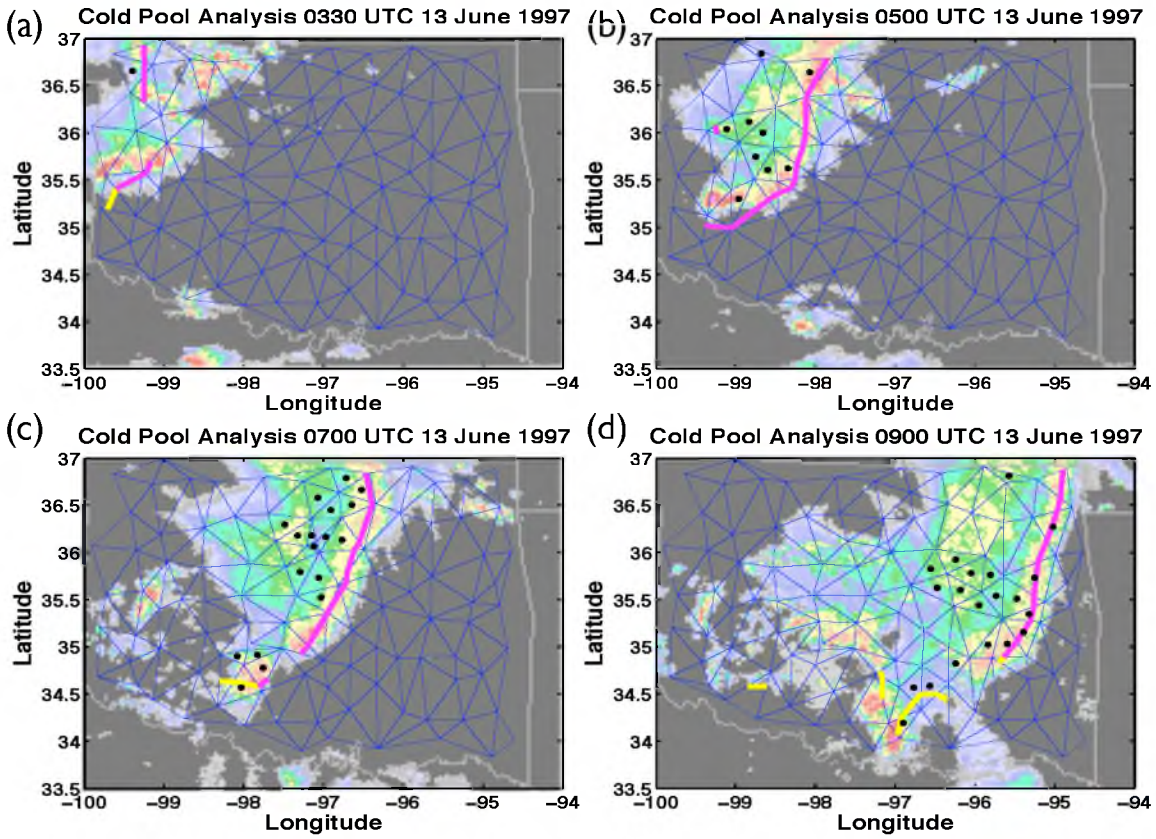

Figure 5.2 – Cold pool analysis for 13 June 1997 (a) 0330 UTC, (b) 0500 UTC, (c) 0700 UTC, and (d) 0900 UTC. Black dots mark triangles that are in cold pools at this time. Fronts from Figure 5.1 are shown for context. Radar images are from the UCAR image archive.

particular triangle. A large active cold pool stretched from the front of the main squall line to the back edge of the stratiform precipitation (Fig 5.2b) in west-central Oklahoma.

From 5 to 7 UTC, the supercell at the south end of the squall line separated from the rest of the line. This separation appears in the form of a gap in the front that was a result of lower FSs (Fig. 5.1c). The southern cell has weaker FSs as one of the triangles marked by the front only meets the lower front score threshold of 3 rather than the higher threshold of 5. The region of strong divergence was primarily concentrated in north central Oklahoma, with a smaller area of strong divergence behind the southern supercell. Cold pools are located in both of these

areas (Fig. 5.2c). In Western Oklahoma a few small convective cells had formed behind the secondary convergence line.

By 9 UTC the southern supercell had progressed southeastward much farther away from the rest of the line (Fig. 5.1d). The stronger portion of the front led the main squall line eastward. The area of strong divergence behind the front was more concentrated on the southern half of the squall line. There was a weaker front (FSs 3+ rather than 5+) to the east of the southern supercell. Behind the supercell to the northwest, trailing convection developed over the previous 2 hrs and eventually merges with the southern supercell (not pictured). There was clear separation between the convergence and divergence in the trailing convection. Overall, the front analysis using FSs performed well at representing the location of the front that would be expected based on the radar images. Despite the separation in the front, the cold pool along the front almost extends from the southern border with Texas to the northern border with Kansas (Fig. 5.2d). Notably the cold pool extends back behind the front in east-central Oklahoma, suggesting a long-lived cold pool. At this time, the main cold pool has been in place for hours and has advanced eastward over time behind the squall line. However, large areas of stratiform precipitation are not classified as in a cold pool because the divergence values were not high enough at this time. Many of the triangles in northeastern Oklahoma would likely be defined as in a cold pool using a different definition relying more on sustained stratiform precipitation or lingering temperature falls.

Observing the change in cold pool area over time allows for greater visualization of the size and time scales of the areas experiencing a cold pool (Fig. 5.3). From roughly 3 to 11 UTC at least one Mesonet triangle resided in a cold pool. The peak size of cold pool area was around 930 UTC at a size of roughly 1.6×10^{10} m^2. Around a third of the cold pool areas retained a cold pool for at least 30 mins, and some triangles, particularly later in the period, retained cold pool status for over an hr.

5.2 15-16 June 2002 Case

Around 18 UTC 15 June, a line of thunderstorms oriented from northwest to southeast was located in north central Kansas and south central Nebraska moving

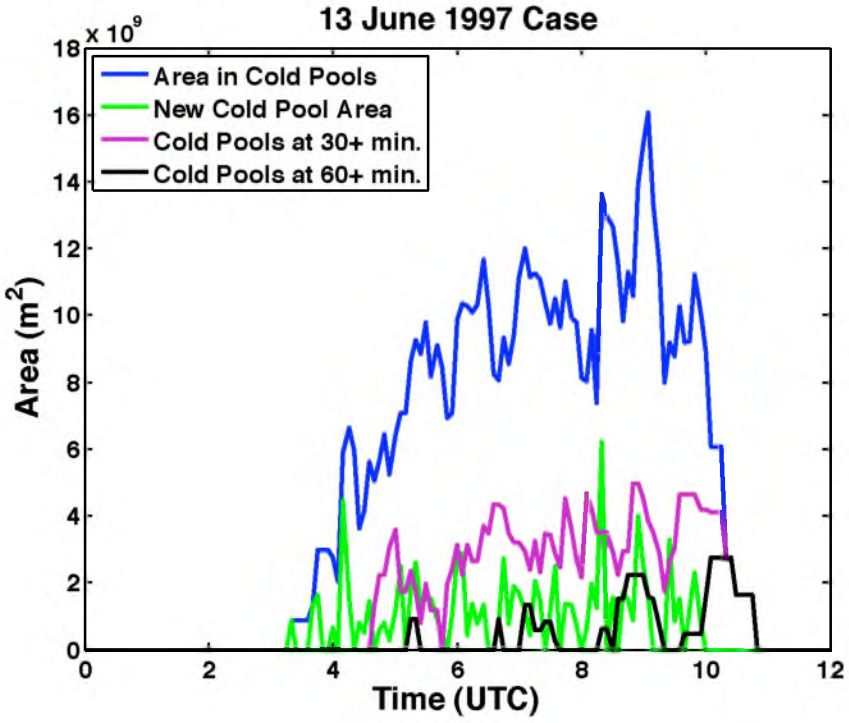

Figure 5.3 – Cold pool areas for the 13 June 1997 0-12 UTC case study. Cold pool areas are shown for total area in cold pools (blue), area that becomes part of a cold pool the given timestep (green), area that has been in a cold pool at least 30 mins (purple), and area that has been in a cold pool at least 60 mins (black).

southeastward. Over the next few hours the system spread out along the front allowing for a much more southwest to northeast oriented storm line to develop as the system moved south to the Oklahoma border. The frontal passage (Fig. 5.4) and cold pool (Fig. 5.5) analysis for this event are shown.

At 0 UTC on the 16^{th} the squall line had just entered the northwest corner of Oklahoma. Very strong convection was present ahead of the line, including triangles over 50 km ahead of the squall line (Fig. 5.4a). Divergence behind the front was present as well as this line had developed into a mature system several hours earlier. The FSs exceeded the strong front threshold. A few isolated triangles along and just behind the line were located in cold pools at this time (Fig. 5.5a). Presumably, the cold pool extends into Kansas.

Ninety mins later the squall line had progressed into the state reaching from almost the southwest corner to the northeast corner of Oklahoma (Fig. 5.4b). The stronger

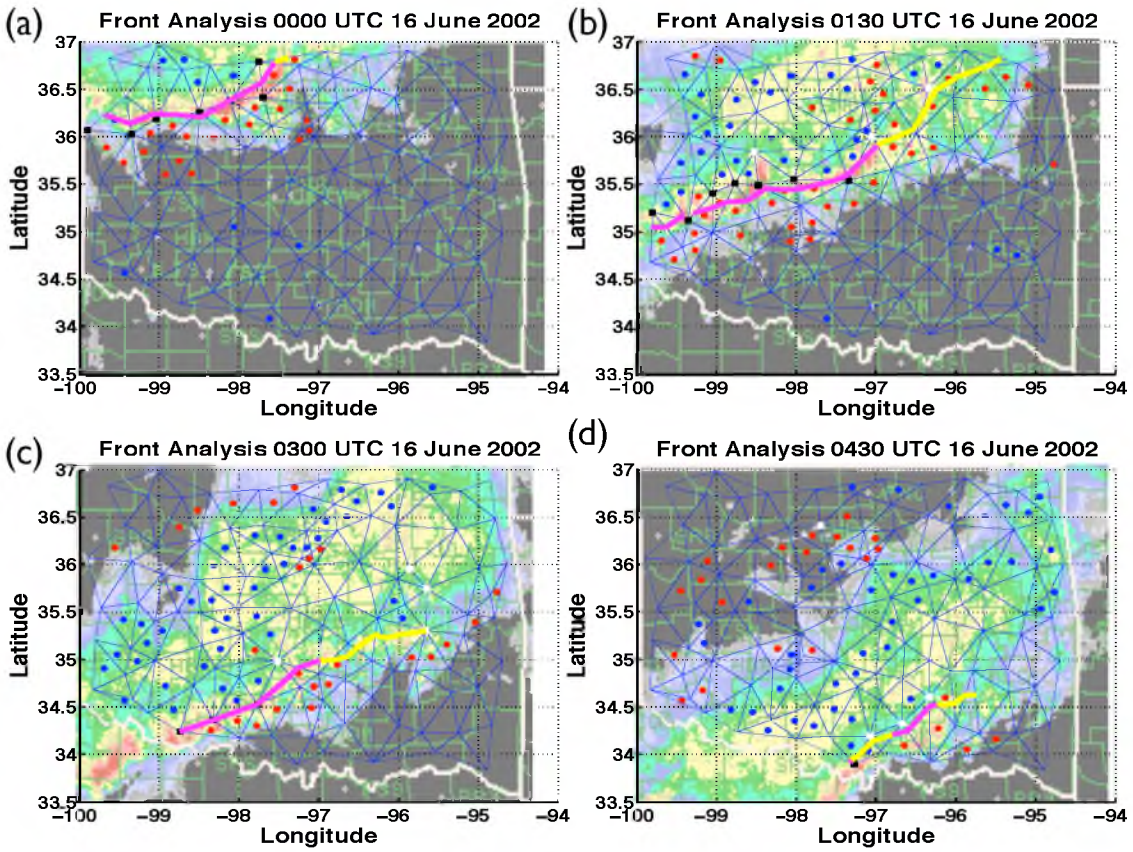

Figure 5.4 – Front analysis for 16 June 2002 (a) 0000 UTC, (b) 0130 UTC, (c) 0300 UTC, and (d) 0430 UTC. Red dots are $D_i < -10^{-4}\text{s}^{-1}$ while blue dots are $D_i > 10^{-4}\text{s}^{-1}$. Yellow lines are frontal passages with FSs of $3 <= \text{FS} < 5$ while magenta lines are frontal passages with FSs of 5+. White squares are stations where at the current timestep the FS is $3 <= \text{FS} < 5$; black squares designate stations currently with FSs at 5+. Radar images are from the UCAR image archive.

radar echoes were in the western half of the squall line, matching up with the stronger FSs. Additionally, the convergence-divergence pattern ahead of and behind the front was more well-defined in the western half of the state though present throughout the squall line. A broad region of heavy stratiform precipitation was located in north central Oklahoma. In that stratiform precipitation region a cold pool was detected far behind the squall line (Fig. 5.5b). Additionally, along the front there was a narrow band of scattered triangles that are in cold pool status, just behind strong convective cells.

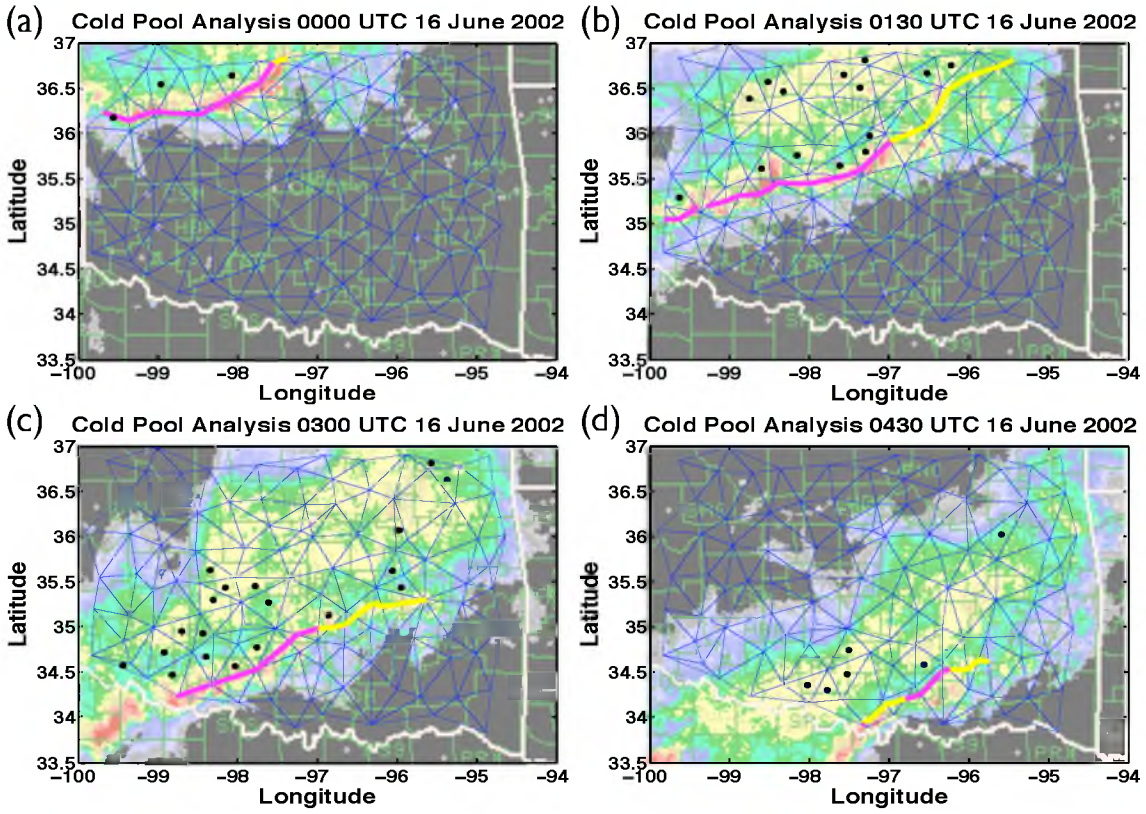

Figure 5.5 – Cold pool analysis for 16 June 2002 (a) 0000 UTC, (b) 0130 UTC, (c) 0300 UTC, and (d) 0430 UTC. Black dots mark triangles that are in cold pools at this time. Fronts from Figure 5.4 are shown for context. Radar images are from the UCAR image archive.

By 3 UTC the eastern half of the squall line had lost much of its strong convection resulting in a front that does not extend all the way to the Arkansas border (Fig. 5.4c), or at least not a front strong enough to meet the minimum threshold in this study. The southwestern corner of Oklahoma still features strong convection, with the line extended into north central Texas. The eastern half of the state has lost most of its divergence behind the line as the convective structure has fallen apart. However, there was still a narrow region of convergence ahead of the squall line. South central Oklahoma had a very large area of divergence behind the front. This extends up into north central Oklahoma with the trailing portion of the stratiform precipitation region. A small line of covergence was present in the stratiform precipitation region in north central Oklahoma with an additional larger line of convergence behind the

stratiform precipitation. There are many triangles experiencing a cold pool in south central Oklahoma behind the squall line (Fig. 5.5c). Extending back several triangles deep, this cold pool covers roughly one eighth of the state. The eastern half of the state has much less cold pool coverage in this analysis though the cold pool does include a couple triangles in the northeast corner where the front had passed over an hr prior. At least a sizable portion of the stratiform precipitation region is likely to be in a cold pool based on other study definitions.

As the system moves farther southeast the strength of the convection in Oklahoma weakened further as the strongest cells to the west moved into Texas. The stratiform region of precipitation was well-defined and contained a large area of divergence behind the remnants of the squall line in Oklahoma (Fig. 5.4d). The line of convergence that was just behind the stratiform precipitation region has fallen farther behind the precipitation though it maintains an almost continuous line through a large portion of the northwest to north central region. The cold pool was concentrated in the south central stratiform precipitation with a few solitary triangles elsewhere in cold pools (Fig. 5.5d).

The cold pool time series shows a slightly larger maximum cold pool area than the first case study with a maximum size of roughly 1.9×10^{10} m^2 (Fig. 5.6). The duration of the cold pools tended to be longer than the first case study. Later in the time period over half the cold pool area comprised of locations which had been in a cold pool for half an hr or more. The cold pool area that was present for at least an hr peaked at roughly 6×10^9 m^2.

5.3 20 May 2011 Case

One of the more notable cases during the Mid-Latitude Continental Convective Clouds Experiment (MC3E) occurred on 20 May 2011 (Fig. 5.7). Scattered convective cells formed in central Oklahoma and by 4 UTC the cells stretched from the Oklahoma-Texas border southwest to the Texas panhandle. These cells organized into a squall line and started to build north through southwestern Oklahoma with the fronts and cold pools tracked with the algorithm (Fig. 5.8).

At 9 UTC (Fig. 5.7a) the front analysis shows a strong front stretching from

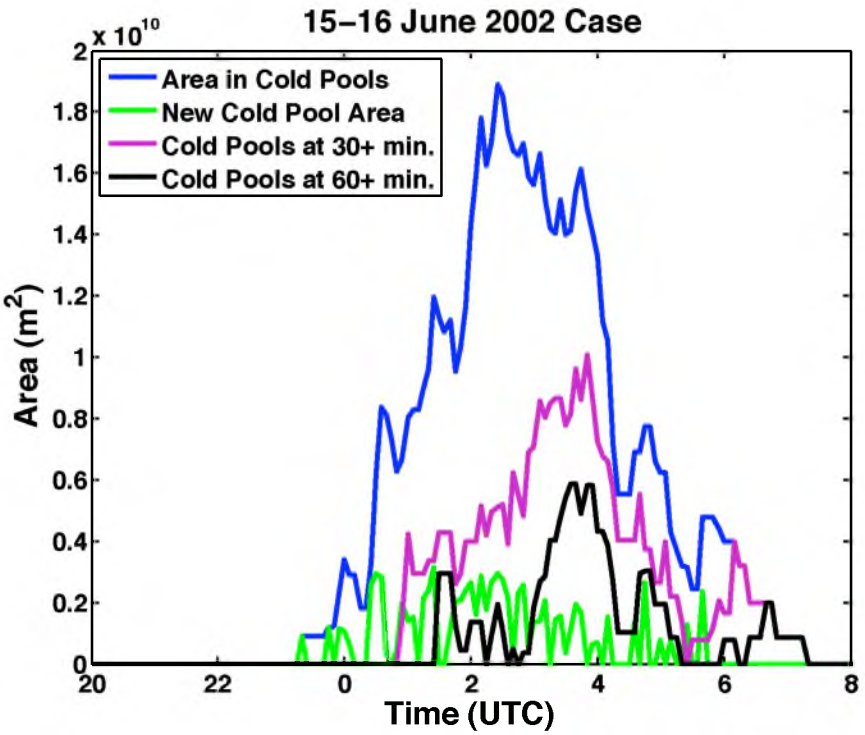

Figure 5.6 – Cold pool areas for the 15-16 June 2002 20-8 UTC case study. Cold pool areas are shown for total area in cold pools (blue), area that becomes part of a cold pool the given timestep (green), area that has been in a cold pool at least 30 mins (purple), and area that has been in a cold pool at least 60 mins (black).

southwestern Oklahoma northward. There was a well-defined squall line as well as convergence ahead of the front and areas of strong divergence behind the front. The structure of the line appears less organized at the northern end of the front as strong convection juts out ahead of the rest of the front. This was due to an isolated thunderstorm from earlier that was merging into the squall line. Due to the merging of that thunderstorm, the frontal boundary was not as well defined in that area and there was only some semblance of a convergence-divergence couplet. Since the line had just developed northward into the area the previous 2 hrs, only two triangles have cold pools present at 9 UTC (Fig. 5.8a).

Over the next couple of hours the squall line builds throughout northern Oklahoma. By 11 UTC the line had developed a bow shape (Fig. 5.7b). Notably, the easternmost part of the bow had lower FSs and contained a break in the high convergence area as well as having slightly lower radar returns. However, a strong

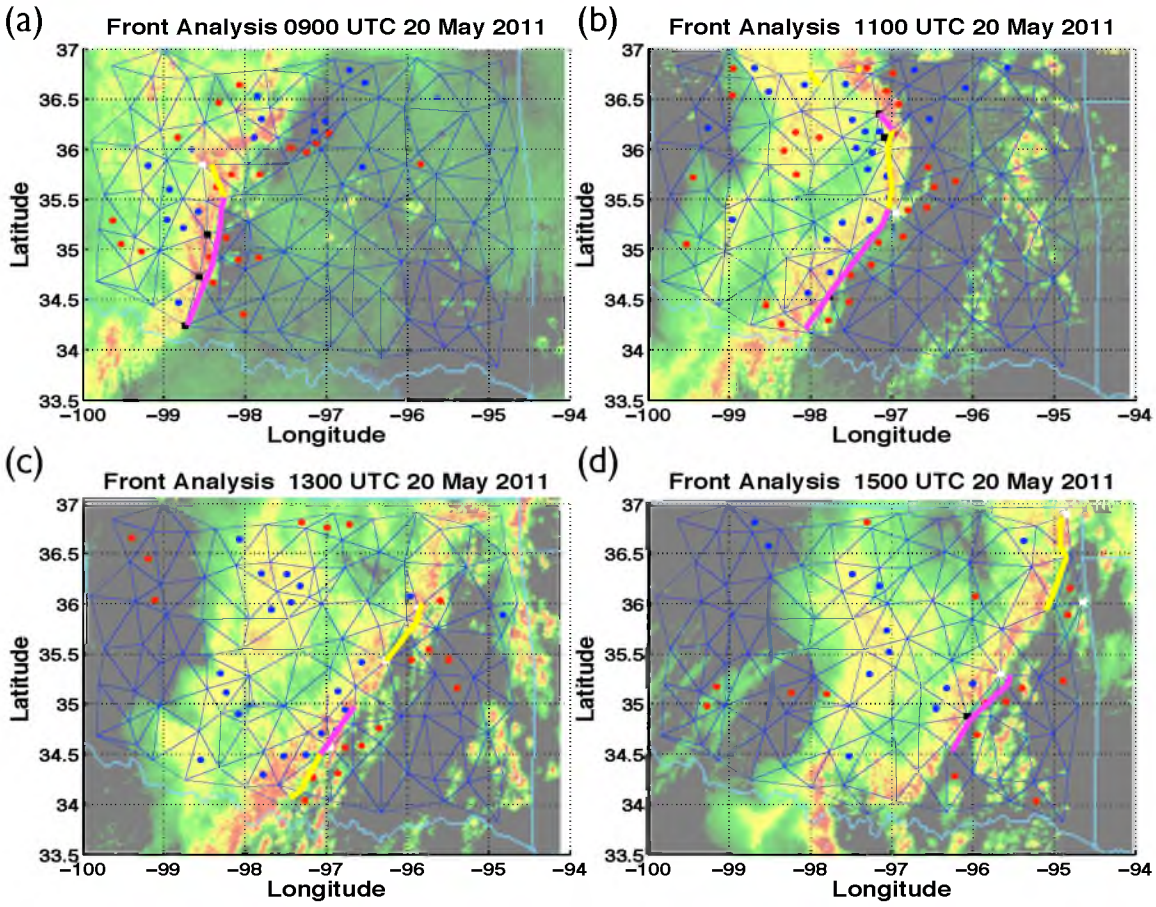

Figure 5.7 – Front analysis for 20 May 2011 (a) 0900 UTC, (b) 1100 UTC, (c) 1300 UTC, and (d) 1500 UTC. Red dots are $D_i < -10^{-4}\text{s}^{-1}$ while blue dots are $D_i > 10^{-4}\text{s}^{-1}$. Yellow lines are frontal passages with FSs of 3 <= FS < 5 while magenta lines are frontal passages with FSs of 5+. White squares are stations where at the current timestep the FS is 3 <= FS < 5; black squares designate stations currently with FSs at 5+. Radar images are from the UCAR image archive, NEXLAB - College of DuPage.

divergence area behind the line did remain intact in that region. The northern part of the squall line has convergence ahead of the front but the FSs at some stations were not high enough to trigger a front to be drawn in that area. Since the northern edge of the front was the most recent to form, it was not strong enough to meet minimum front score thresholds. A distinct line of triangles containing cold pools stretches through over two thirds the width of the state just behind the front (Fig. 5.8b). Unlike the 1997 case, the cold pool does not extend as far behind the front.

From 11 to 13 UTC the northern part of the bow began to break apart. Convection

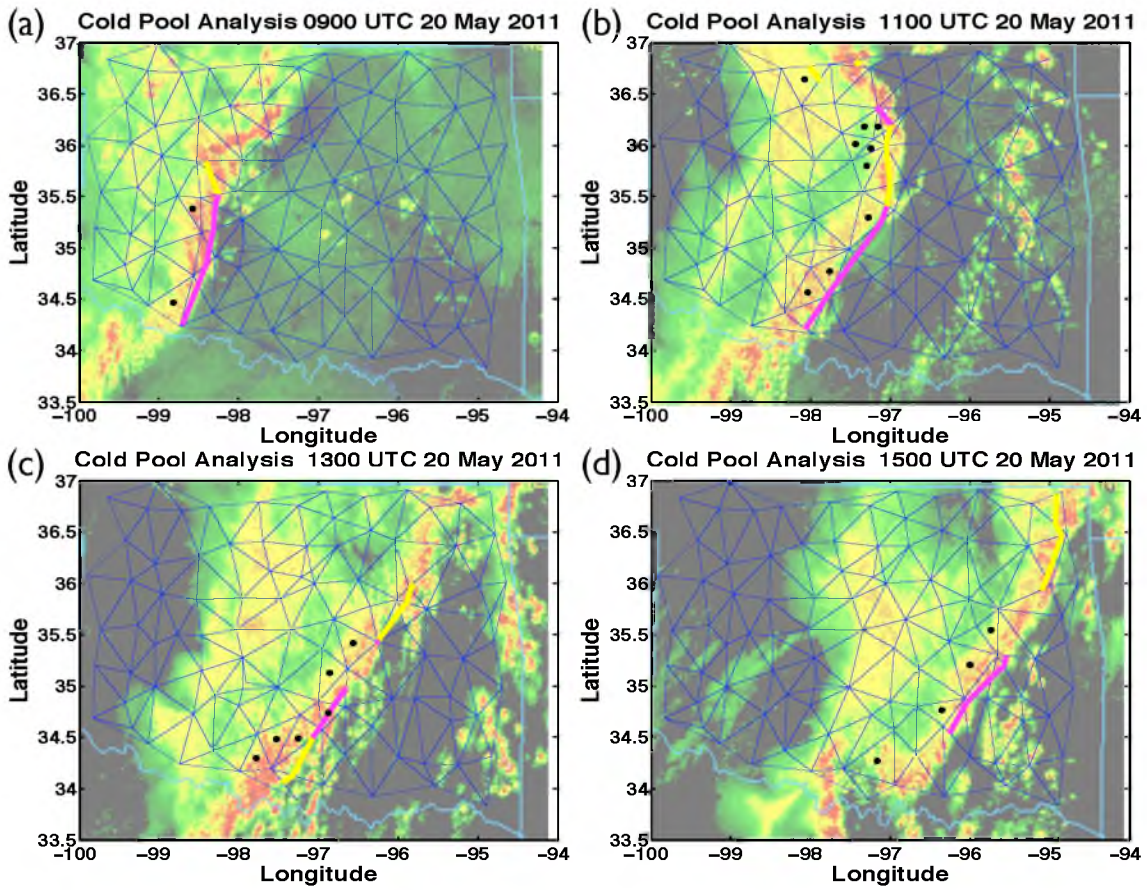

Figure 5.8 – Cold pool analysis for 20 May 2011 (a) 0900 UTC, (b) 1100 UTC, (c) 1300 UTC, and (d) 1500 UTC. Black dots mark triangles that are in cold pools at this time. Fronts from Figure 5.7 are shown for context. Radar images are from the UCAR image archive.

ahead of the front led to a more scattered area of thunderstorms in northeastern Oklahoma (Fig. 5.7c) as well as thunderstorms popping up several counties east of the squall line. The structure of the line was oriented southwest to northeast by 13 UTC. The front analysis retained the southern half of the front as meeting the strong front threshold while a few triangles on the northern end have the lower FS threshold met. Similarly the cold pool area has decreased as only the southern Oklahoma portion of the front managed to exceed the divergence threshold (Fig. 5.8c). This case shows a clear signal of steady forward movement of the cold air mass production region classified by downdrafts while the stratiform precipitation region behind is a cold air maintenance region.

The front continues through the state, exiting through northeastern Oklahoma around 15 UTC (Fig. 5.7d) while the southern end of the front exits the state a couple hrs later before a second line of storms moves into southeastern Oklahoma (not shown). There were no areas of strong divergence behind the northeastern Oklahoma portion of the front. The cold pool covered only a few triangles in southeastern Oklahoma (Fig. 5.8d).

The cold pool time series showed a longer lasting period from initial to final cold pool and a lower maximum cold pool area that only reached roughly 9×10^9 m^2 (Fig. 5.9). There are frequent jumps in the amount of area covered by cold pools. Many of the cold pools lasted half an hr; however, very few triangles maintained a cold pool for at least an hr. Considering the narrow width of the divergence region behind the storm line and the speed of the front, this result was expected.

5.4 24-25 May 2011 Case

The final case study is another system that occurred during the MC3E experiment a few days after the previous case. On 24 May the 18 UTC sounding (not shown, UCAR archive) from Norman, Oklahoma (KOUN) had strong southerly winds at low-levels veering with height. A strong stable layer at roughly 825 mb was in place; however, low-level moisture and an unstable mid-level resulted in CAPE values over 2500 Jkg^{-1}. The Storm Prediction Center (SPC) had issued a high risk convective outlook for central and northeastern Oklahoma.

By 20 UTC the first thunderstorm cells had formed, rapidly developing into severe thunderstorms with a threat of tornadoes. The frontal passage (Fig. 5.10) and cold pool (Fig. 5.11) analysis had some difficulty capturing the front and any associated cold pool with these thunderstorms due to the low resolution of the Mesonet station grid (Fig. 5.10a). There was a large region of convergence both ahead of and behind the supercells at this time. The front, although strong, did not extend throughout all of the supercells, and only one triangle observed a cold pool (Fig. 5.11a).

Over the next couple hrs, more cells had flared up and a clear north-south line had formed (Fig. 5.10b) though there were gaps between the cells that made up the line. There was only a slight signature of the usual convergence-divergence pattern

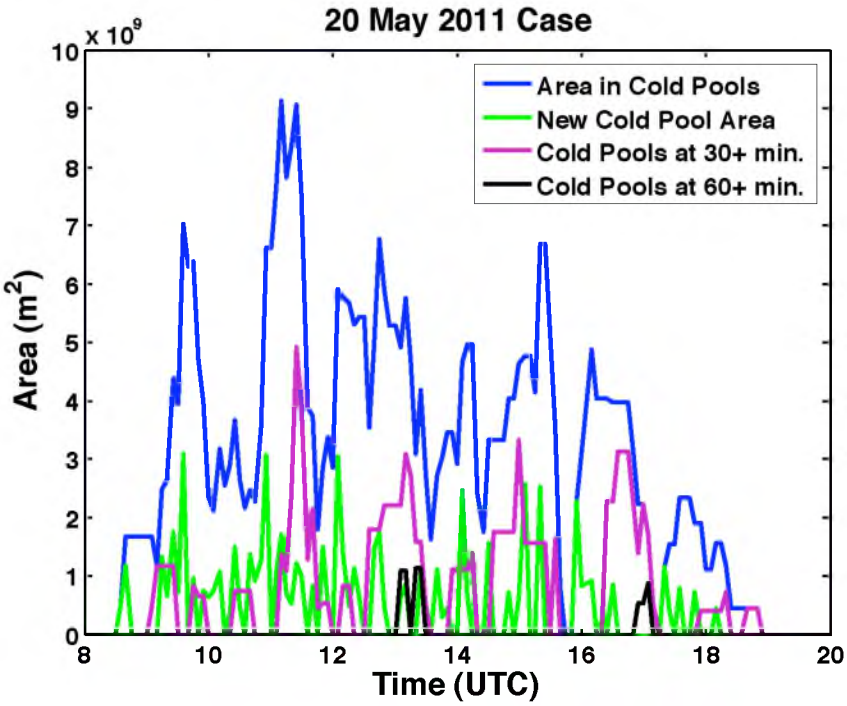

Figure 5.9 – Cold pool areas for the 20 May 2011 8-20 UTC case study. Cold pool areas are shown for total area in cold pools (blue), area that becomes part of a cold pool the given timestep (green), area that has been in a cold pool at least 30 mins (purple), and area that has been in a cold pool at least 60 mins (black).

ahead of and behind the front, likely, though not necessarily, a result of the strong rotation in tornadoes, or systems capable of potentially producing tornadoes. At this point multiple tornadoes had formed, including one that struck the El Reno Mesonet station at 2120 UTC recording a maximum wind gust of 151 mph. Only a few stations in north central and northwestern Oklahoma observed cold pools at the time (Fig. 5.11b). Strong rotation tends to lead to surface inflow from all directions, reducing the likelihood of divergence and cold pools behind a front.

By 0 UTC, however, the squall line was straighter and had fewer, smaller gaps between individual storm cells (Fig. 5.10c). A convergence-divergence distribution ahead of and behind the front was more well-defined in the north central Oklahoma line and the smaller, weaker (in terms of front strength) line in south central Oklahoma. A large region of convergence is present in western Oklahoma where a secondary front was present that lacked precipitation. Cold pool coverage had grown

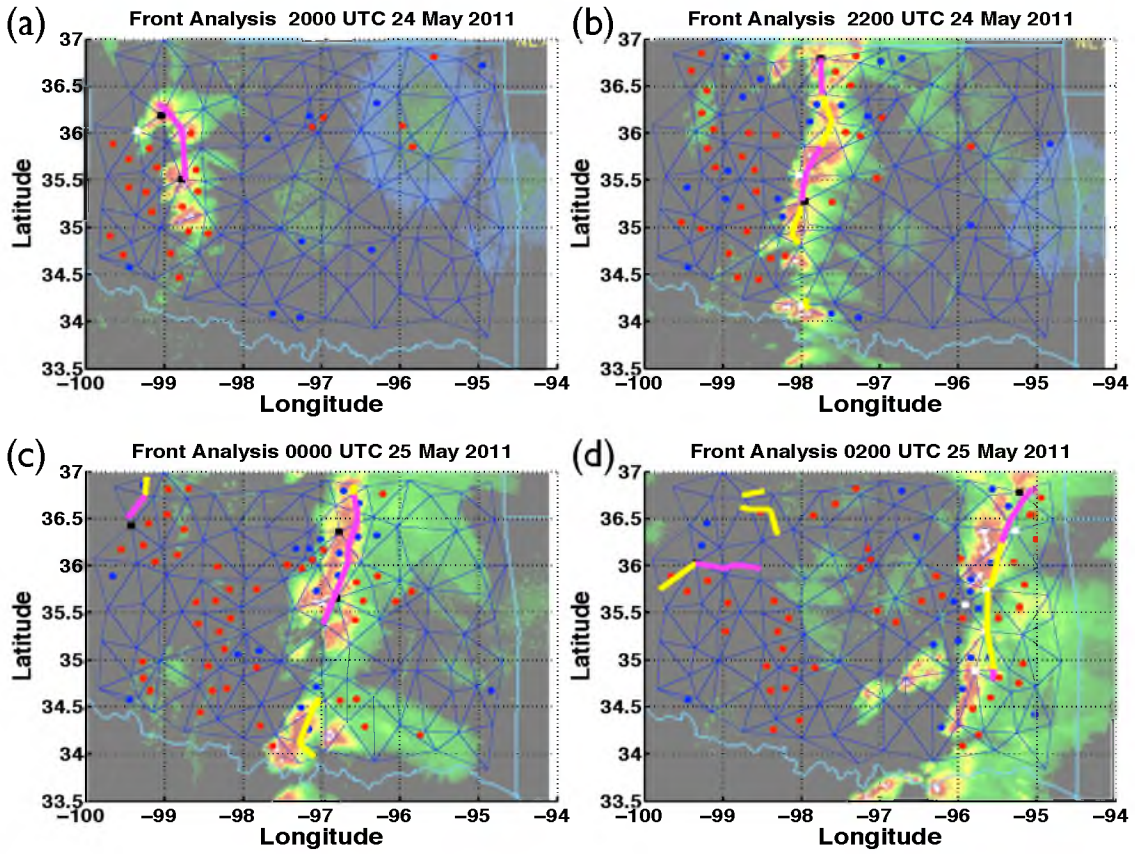

Figure 5.10 – Front analysis for 24 May 2011 (a) 2000 UTC, (b) 2200 UTC, 25 May 2011 (c) 0000 UTC, and (d) 0200 UTC. Red dots are $D_i < -10^{-4}\text{s}^{-1}$ while blue dots are $D_i > 10^{-4}\text{s}^{-1}$. Yellow lines are frontal passages with FSs of 3 <= FS < 5 while magenta lines are frontal passages with FSs of 5+. White squares are stations where at the current timestep the FS is 3 <= FS < 5; black squares designate stations currently with FSs at 5+. Radar images are from the UCAR image archive, NEXLAB - College of DuPage.

behind the main line in central Oklahoma (Fig. 5.11d). Additionally, one triangle was marked as in a cold pool in the northwest corner of Oklahoma. Generally, the lack of stratiform precipitation makes it likely that this case is closer to what other studies would identify in terms of cold pool area compared to the other cases in this chapter.

As the main front progressed further eastward the strength of the front began to weaken slightly with regards to FSs (Fig. 5.10d). However, convection was still intense with radar echoes reaching up to 60 dBZ still present. The fronts in western Oklahoma

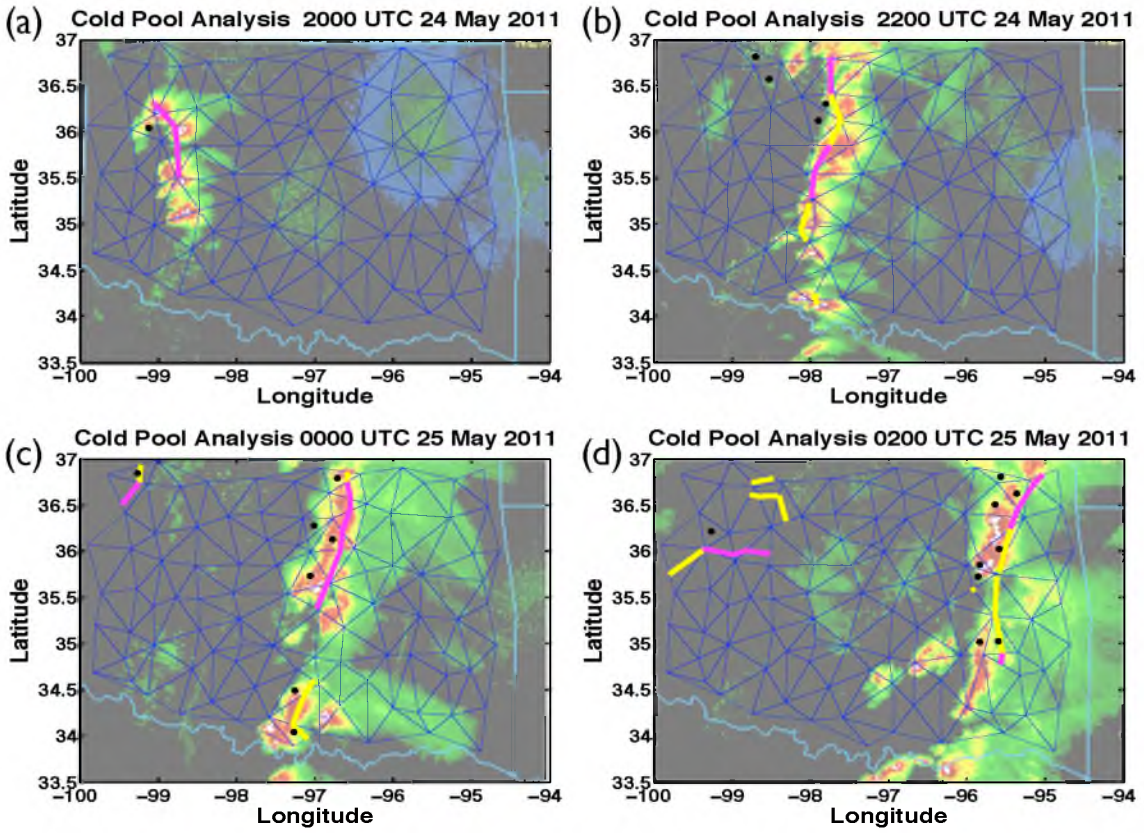

Figure 5.11 – Cold pool analysis for 24 May 2011 (a) 2000 UTC, (b) 2200 UTC, 25 May 2011 (c) 0000 UTC, and (d) 0200 UTC. Black dots mark triangles that are in cold pools at this time. Fronts from Figure 5.10 are shown for context. Radar images are from the UCAR image archive.

had a disorganized structure and covered more area at the time. The cold pools at 2 UTC remained just behind the main front with one triangle in western Oklahoma in a cold pool as well (Fig. 5.11d). Radar coverage in northwestern Oklahoma was sparse by comparison, though the secondary line does not appear to develop precipitation as it moves throughout the state the next few hours. At 3 UTC (not shown) there was a faint green line visible on the radar signifying this secondary front.

The cold pool time series for this final case study showed a maximum cold pool area of just over 1.1×10^{10} m^2 (Fig. 5.12). The entire period with cold pools present lasted approximately 10 hrs. The cold pools were rather short in duration with few lasting half an hr and only one triangle retaining a cold pool over an hr. Cold pools later in the event had longer durations than cold pools in the first half of the event,

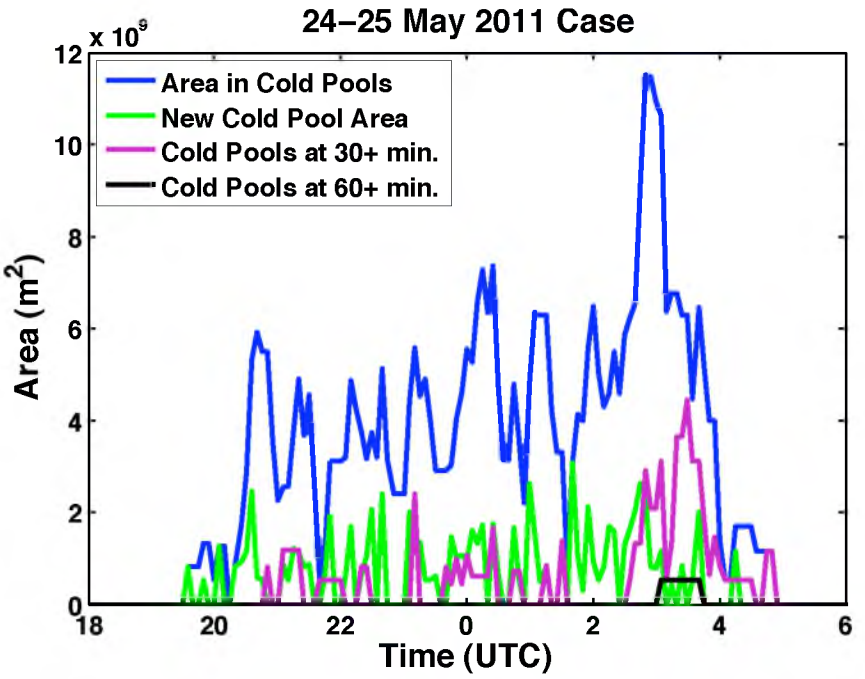

Figure 5.12 – Cold pool areas for the 24-25 May 2011 18-6 UTC case study. Cold pool areas are shown for total area in cold pools (blue), area that becomes part of a cold pool the given timestep (green), area that has been in a cold pool at least 30 mins (purple), and area that has been in a cold pool at least 60 mins (black).

a result of the increased organization of the convergence-divergence gradient across the front over time.

CHAPTER 6

RESULTS: 15-YR CLIMATOLOGY OF FRONTS AND COLD POOLS

The 1997-2011 period of Oklahoma Mesonet data allowed for 15 yrs of frontal passages and cold pools to be analyzed with statistics gathered on these frontal passages and cold pools. This analysis processed almost one billion observations from the Mesonet. Frontal passage and cold pool statistics are covered for: (1). Variable changes (T, P, q_v, and hc_p^{-1}), (2). Convergence/divergence (3). Seasonal distribution, (4). Diurnal distribution, and (5). Geographic distribution.

6.1 Variable Changes (T, P, q_v, and h/c_p)

For each frontal passage at a Mesonet triangle the three corners of the triangle were included in the statistics of changes in key variables as a result of the frontal passage. Those variables are temperature (T), pressure (P), water vapor mixing ratio (q_v), and moist static energy in temperature units (hc_p^{-1}). The changes in these four variables during all frontal passages (FS3+) and strong frontal passages (FS5+) (Table 6.1) and frontal passages which result in cold pools and strong cold pools are shown (Table 6.2).

The temperature difference is calculated by subtracting the highest temperature within 30 mins before a frontal passage at a station from the lowest temperature within 2 hrs after the frontal passage. Pressure differences are calculated by subtracting the lowest pressure within 30 mins before the frontal passage from the highest pressure within 2 hrs after the frontal passage. The times before and after the front are not necessarily the same for temperature and pressure changes. Δq_v and Δhc_p^{-1}, however, are calculated at the same timestep as ΔT. This was chosen because T and q_v are directly involved in calculations of hc_p^{-1}.

Table 6.1 – Average ΔT, ΔP, Δq_v, and Δhc_p^{-1} for all frontal passage (FS3+ / FS5+).

Season	ΔT (K)	ΔP (mb)	Δq_v ($\mathbf{gkg^{-1}}$)	Δhc_p^{-1} (K)
Spring (MAM)	-5.8/-7.7	2.8/3.6	-1.5/-2.9	-9.2/-14.8
Summer (JJA)	-6.1/-7.7	2.0/2.5	-0.6/-1.0	-7.1/-10.2
Fall (SON)	-6.2/-8.4	2.4/3.1	-1.5/-2.8	-9.6/-15.3
Winter (DJF)	-6.6/-10.2	2.9/4.4	-1.2/-2.7	-9.5/-17.1
Annual	-6.1/-8.1	2.5/3.2	-1.1/-2.1	-8.7/-13.4

Table 6.2 – Average ΔT, ΔP, Δq_v, and Δhc_p^{-1} during frontal passages that yield cold pools (FS3+ / FS5+).

Season	ΔT (K)	ΔP (mb)	Δq_v ($\mathbf{gkg^{-1}}$)	Δhc_p^{-1} (K)
Spring (MAM)	-5.8/-7.5	2.9/3.5	-1.7/-2.8	-10.1/-14.6
Summer (JJA)	-6.2/-7.7	2.0/2.5	-0.8/-1.0	-8.1/-10.3
Fall (SON)	-6.3/-8.3	2.6/3.1	-1.6/-2.5	-10.3/-14.6
Winter (DJF)	-7.1/-10.3	3.5/4.5	-1.5/-2.8	-10.9/-17.1
Annual	-6.2/-8.0	2.6/3.1	-1.3/-2.0	-9.5/-13.0

Generally, results for all frontal passages, including those which did not lead to cold pools, were fairly similar to those for only fronts that led to cold pools. The magnitude of all of the variable changes increased on average for fronts with cold pools rather than fronts without cold pools if all fronts (FS3+) are considered. However, the magnitude of all of the variable changes decreased on average for strong fronts (FS5+) with cold pools compared to strong fronts without cold pools.

Temperature shows lower average temperature falls in spring and higher temperature falls in winter than average. Average pressure rises have a distinct minimum in magnitude in summer while during the winter pressure changes are largest on average. Water vapor mixing ratio decreases a much smaller amount in summer on average compared to the other three seasons. Moist static energy has the smallest average decrease in summer and largest average decrease in winter. Since moist static energy is a function of temperature and water vapor mixing ratio, these results reveal those dependencies in summer differences are much lower than the other seasons (a q_v influence), and winter differences are much higher than the other seasons (a T

influence).

When plotted ΔT and ΔP show low correlation, -0.27, with fronts primarily taking the form of 3-7 K temperature drops with 0-4 mb pressure rises (Fig. 6.1). Correlations between the four variable changes were calculated for all fronts (Table 6.3) and fronts that yielded cold pools (Table 6.4). Summer correlations are lower for all combinations involving temperature while winter correlations involving temperature are higher. ΔP correlations with Δq_v and $\Delta h c_p^{-1}$ were lowest in summer and winter. The correlation between Δq_v and $\Delta h c_p^{-1}$ is roughly the same all year. Notably, the correlation between ΔT and Δq_v is slightly negative in summer while it is positive for all other seasons. Also, the strong front correlations between ΔP and Δq_v are positive in the winter while it is negative for the other seasons. Correlations between Δq_v and $\Delta h c_p^{-1}$ were higher than correlations between ΔT and $\Delta h c_p^{-1}$, suggesting that Δq_v has a stronger influence on $\Delta h c_p^{-1}$ than ΔT.

Differences are minimal between the correlations for frontal passages and only frontal passages that yield cold pools. Surprisingly, temperature correlations for stronger frontal passages during the summer have lower values than temperature correlations involving all frontal passages. These correlations suggest that stronger fronts have more varied structure than weaker fronts, possibly a result of the greater likelihood of convective rather than stratiform precipitation events in the summer.

6.2 Convergence/Divergence

It is expected that ahead of a frontal passage convergence would be likely to occur while behind a frontal passage divergence would be likely to occur. Cold pools are marked by the presence of significant divergence associated with a frontal passage, generally a short time after frontal passage occurs. As noted earlier, the divergence values were averaged over 15 mins to smooth out some timing discrepancies that may occur in a study with large station spacing.

The divergence values were calculated at the beginning, middle, and end of each triangles' frontal passage. The beginning of a frontal passage is defined as the timestep where the first of the three triangle corner points reaches a local maximum front score. The end of a frontal passage is the timestep where the third of the three triangle corner

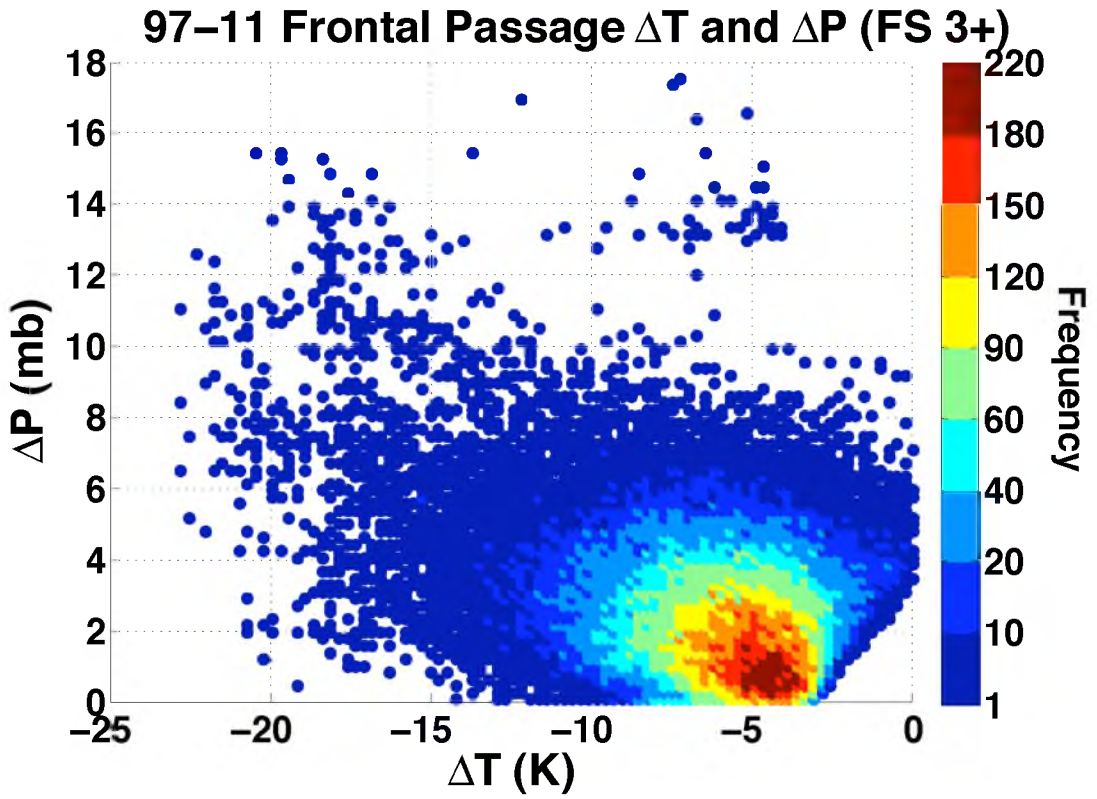

Figure 6.1 – ΔP vs ΔT for all frontal passages at triangles in the Oklahoma Mesonet from the 1997-2011 period. The colorbar represents the frequency of occurrence. The correlation is -0.27.

points reaches a local maximum front score. The middle of the frontal passage is the halfway point between the first and last timestep. If there are an even number of timesteps then the two middle divergence values are averaged.

The divergence values for all frontal passages were calculated and shown in Table 6.5. On average, the triangles did have strong convergence ($D_i < -10^{-4}$ s^{-1}) as the front initially reaches the triangle. The magnitude of convergence had small differences between seasons, with the convergence for all fronts being slightly weaker in winter and the convergence for strong fronts being stronger in fall and spring than summer and winter. For fronts at the middle of a triangle, there was a large seasonal difference. Summer frontal passages had divergence on average at the middle of a frontal passage while the other three seasons maintained convergence. At the end of a frontal passage summer had the strongest divergences on average while winter had

Table 6.3 – Correlations between ΔT, ΔP, Δq_v, and Δhc_p^{-1} for all frontal passages (FS3+ / FS5+).

Season	ΔT,ΔP	ΔT,Δq_v	ΔT,Δhc_p^{-1}	ΔP,Δq_v	ΔP,Δhc_p^{-1}	Δq_v,Δhc_p^{-1}
Spring (MAM)	-0.32/-0.44	0.36/0.31	0.61/0.61	-0.20/-0.15	-0.24/-0.28	0.94/0.94
Summer (JJA)	-0.15/-0.06	-0.01/-0.11	0.33/0.19	-0.13/-0.14	-0.17/-0.15	0.92/0.95
Fall (SON)	-0.23/-0.17	0.42/0.41	0.65/0.65	-0.32/-0.22	-0.33/-0.24	0.95/0.96
Winter (DJF)	-0.41/-0.38	0.54/0.47	0.80/0.77	-0.14/+0.17	-0.28/-0.03	0.92/0.93
Annual	-0.28/-0.32	0.28/0.22	0.58/0.53	-0.20/-0.17	-0.25/-0.25	0.93/0.94

Table 6.4 – Correlations between ΔT, ΔP, Δq_v, and Δhc_p^{-1} for frontal passages which yield cold pools (FS3+ / FS5+).

Season	ΔT,ΔP	ΔT,Δq_v	ΔT,Δhc_p^{-1}	ΔP,Δq_v	ΔP,Δhc_p^{-1}	Δq_v,Δhc_p^{-1}
Spring (MAM)	-0.32/-0.46	0.38/0.31	0.65/0.61	-0.19/-0.18	-0.27/-0.31	0.95/0.94
Summer (JJA)	-0.13/-0.04	-0.02/-0.12	0.33/0.19	-0.12/-0.13	-0.18/-0.15	0.93/0.95
Fall (SON)	-0.22/-0.18	0.40/0.41	0.67/0.65	-0.29/-0.25	-0.34/-0.28	0.95/0.96
Winter (DJF)	-0.44/-0.43	0.55/0.46	0.83/0.77	-0.07/+0.15	-0.26/-0.08	0.92/0.92
Annual	-0.27/-0.32	0.25/0.19	0.57/0.51	-0.20/-0.19	-0.26/-0.28	0.93/0.94

Table 6.5 – Divergence values at the beginning, middle, and end of all triangle frontal passages experienced by Mesonet triangles from 1997-2011 by season (FS3+ / FS5+) in s^{-1}.

Season	Beg. Div.	Mid. Div.	End. Div.
Spring (MAM)	-1.40E^{-4}/-2.00E^{-4}	-1.55E^{-5}/-2.55E^{-5}	6.50E^{-5}/8.08E^{-5}
Summer (JJA)	-1.32E^{-4}/-1.72E^{-4}	1.87E^{-5}/2.47E^{-5}	1.24E^{-4}/1.61E^{-4}
Fall (SON)	-1.37E^{-4}/-2.02E^{-4}	-3.12E^{-5}/-5.30E^{-5}	5.75E^{-5}/8.03E^{-5}
Winter (DJF)	-1.09E^{-4}/-1.75E^{-4}	-3.52E^{-5}/-6.36E^{-5}	2.30E^{-5}/2.94E^{-5}
Annual	-1.32E^{-4}/-1.87E^{-4}	-1.10E^{-5}/-1.83E^{-5}	7.50E^{-5}/1.01E^{-4}

the weakest divergence. End-of-front divergence for summer was roughly the same as the beginning-of-front convergence. For the other three seasons the magnitude of convergence at the beginning of a frontal passage was much larger than the magnitude of divergence at the end of a frontal passage.

Divergence values for only the frontal passages which yielded cold pools are shown in Table 6.6. Since cold pools require the divergence threshold to be exceeded, the end divergence and middle divergence values are much higher than for all frontal passages. The seasonal pattern remains; however, as summer has the highest divergence in the middle and end of frontal passages while winter has the lowest divergence for the end of frontal passages. Notable is the fact that the beginning divergence values show roughly the same average convergence value for cold pools as is the case for all frontal passages with only a very slight reduction. This suggests that divergence behind a front is not significantly dependent on convergence ahead of a front.

6.3 Seasonal Distribution

The seasonal distribution of frontal passages and cold pools was determined. For this calculation, instead of the stations of each triangle that experienced a front or cold pool being summed, it is the number of triangles that experienced a front or cold pool that is summed (Table 6.7). There were more frontal passages and cold pools during the summer than the other seasons. Winter had the fewest number of frontal passages and cold pools. Frontal passages during the summer also had the highest percentage of fronts leading to cold pools. Stronger fronts resulted in higher odds of cold pool formation as expected.

Table 6.6 – Divergence values at the beginning, middle, and end of triangle frontal passages yielding cold pools experienced by Mesonet triangles from 1997-2011 by season (FS3+ / FS5+) in s^{-1}.

Season	Beg. Div.	Mid. Div.	End. Div.
Spring (MAM)	-1.35E^{-4}/-1.86E^{-4}	3.47E^{-5}/2.77E^{-5}	1.26E^{-4}/1.36E^{-4}
Summer (JJA)	-1.29E^{-4}/-1.70E^{-4}	4.69E^{-5}/4.63E^{-5}	1.62E^{-4}/1.89E^{-4}
Fall (SON)	-1.35E^{-4}/-1.98E^{-4}	2.11E^{-5}/1.90E^{-6}	1.27E^{-4}/1.45E^{-4}
Winter (DJF)	-9.82E^{-5}/-1.62E^{-4}	2.51E^{-5}/4.22E^{-5}	9.58E^{-5}/9.66E^{-5}
Annual	-1.29E^{-4}/-1.78E^{-4}	3.68E^{-5}/3.02E^{-5}	1.38E^{-4}/1.58E^{-4}

Table 6.7 – Number of frontal passages and cold pools experienced by Mesonet triangles from 1997-2011 by season (FS3+ / FS5+).

Season	# Fronts	# Cold Pools	% Fronts w/ Cold Pools
Spring (MAM)	23,811/8,329	13,820/5,397	58%/65%
Summer (JJA)	22,785/9,014	18,083/7,855	79%/87%
Fall (SON)	13,009/4,442	6,645/2,620	51%/59%
Winter (DJF)	12,539/3,843	4,329/1,530	35%/40%
Annual	72,144/25,628	42,877/17,402	59%/68%

A factor influencing the seasonal difference is the dependence of evaporative precipitation on temperature. An increase in temperature leads to an increase in evaporative precipitation. As a result, summer months are more highly influenced by this effect explaining a portion of the seasonal difference, particularly for cold pools. Additionally, seasonal variation between convective and stratiform precipitation is likely an influence in this result.

6.4 Diurnal Distribution

The diurnal distributions of frontal passages and cold pools were calculated as well. Since data were collected every 5 minutes, the number of fronts at all triangles were added up over hourly periods (0000-0055 UTC, 0100-0155 UTC,...,2300-2355 UTC). Seasons were defined as: MAM for spring, JJA for summer, SON for fall, and DJF for winter.

There is a significant seasonal difference in the diurnal distribution of frontal passages (Fig. 6.2). In the summer (Fig. 6.2b) there is a large spike in frontal passage

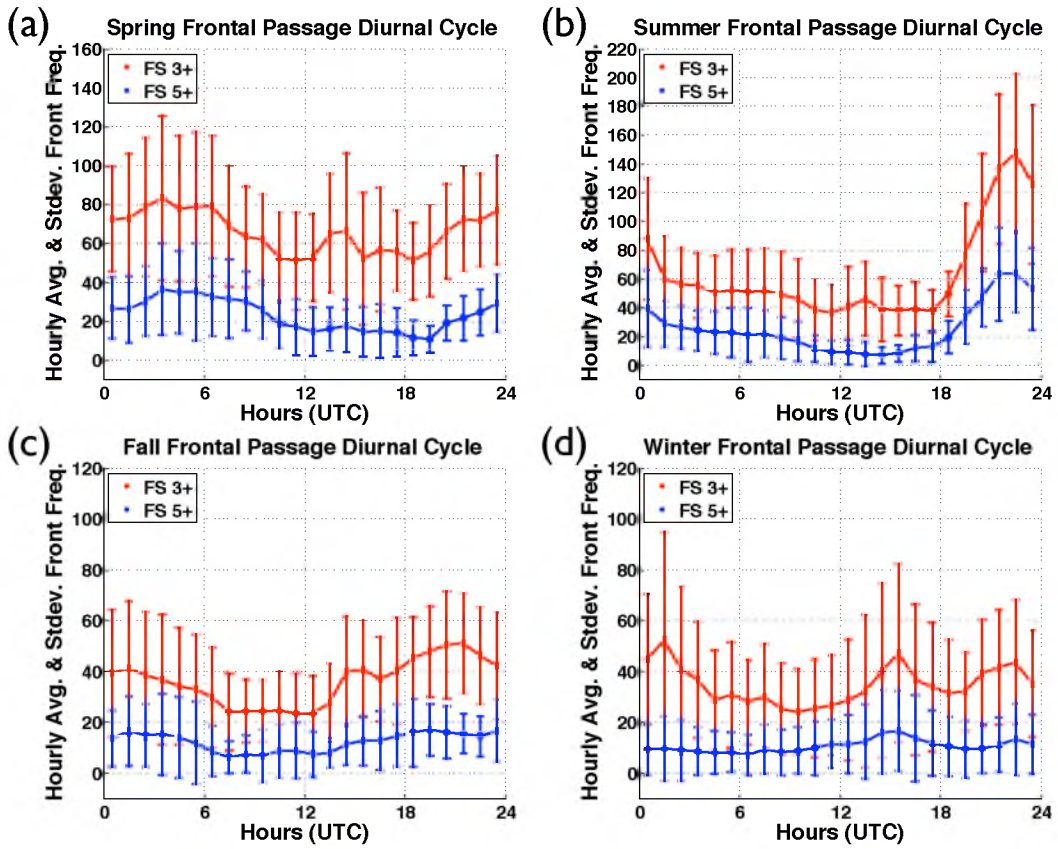

Figure 6.2 – Seasonally averaged diurnal cycle (in UTC time) of all frontal passages at triangles in the Oklahoma Mesonet from the 1997-2011 period along with standard deviations. Results are shown for (a) spring, (b) summer, (c), fall, and (d) winter for all frontal passages (red) and strong frontal passages (blue).

frequency in the afternoon from 20-1 UTC with frontal passage frequencies twice as high as the rest of the day. The other three seasons have much smaller variation in the diurnal cycle. Presumably, more years would make for more smoothing of the data.

The standard deviations are rather large, a result that comes from the tendency for frontal passages to largely appear at the same time for a given system moving through Oklahoma since a single synoptic front can sweep through most of the counties in a few hours. Despite it being impossible for there to be more strong frontal passages than total fronts, the standard deviations of 3+ fronts and 5+ fronts do overlap some which means it can be expected that some years have more strong fronts in a given hour of the day than other years would have total fronts in that hour. Likewise, it

is expected that there are years where total frontal passages are less common than strong frontal passages are for a given hour in a different year. Notably, the standard deviation for strong frontal passages extends below 0 which is impossible and a result of a low average with large outliers on the high side yielding a large standard deviation.

The diurnal distribution of cold pools is very similar to that for frontal passages (Fig. 6.3). The summer has a large diurnal cycle while the spring and fall have smaller amplitude diurnal cycles. The winter has almost no change at all throughout the diurnal cycle. The difference between the highest and lowest average frequency hour for spring, summer, and fall, are all over 50%. Summer's maximum difference is over 200% higher in the most frequent hour compared to the least frequent hour.

The percentage of frontal passages yielding cold pools was also calculated (Fig. 6.4). For most hours of the day in each of the 4 seasons the percentage of strong fronts resulting in cold pools was higher than the percentage of all fronts resulting in cold pools. Consistently throughout the year, it was the evening hours that had the largest spread between all and strong frontal passages leading to cold pools.

In the spring (Fig. 6.4a) roughly 60% of fronts resulted in cold pools throughout most of the day. The morning hours were the exception with the percentage dropping below 50% for several hours (15-19 UTC). The summer (Fig. 6.4b) had the highest rate of frontal passages yielding cold pools, exceeding 90% in the evening hours for strong frontal passages. There is a much slighter drop in the percentage of frontal passages yielding cold pools in the morning hours for the summer than there was in the spring, and this drop did not occur for strong frontal passages. No individual hour falls below 70% of total fronts yielding cold pools. In the fall evening hours (Fig. 6.4c) 60% of frontal passages and 75% of strong frontal passages resulted in cold pools. During the day these percentages fell to between 40 and 55% until the mid-afternoon. In the winter (Fig. 6.4d) the rate of frontal passages resulting in cold pools is consistent throughout the day between 30 and 40%.

6.5 Geographic Distribution

Finally, the geographic distributions of frontal passages and cold pools across the Mesonet were computed. An issue that became apparent was the dependence of

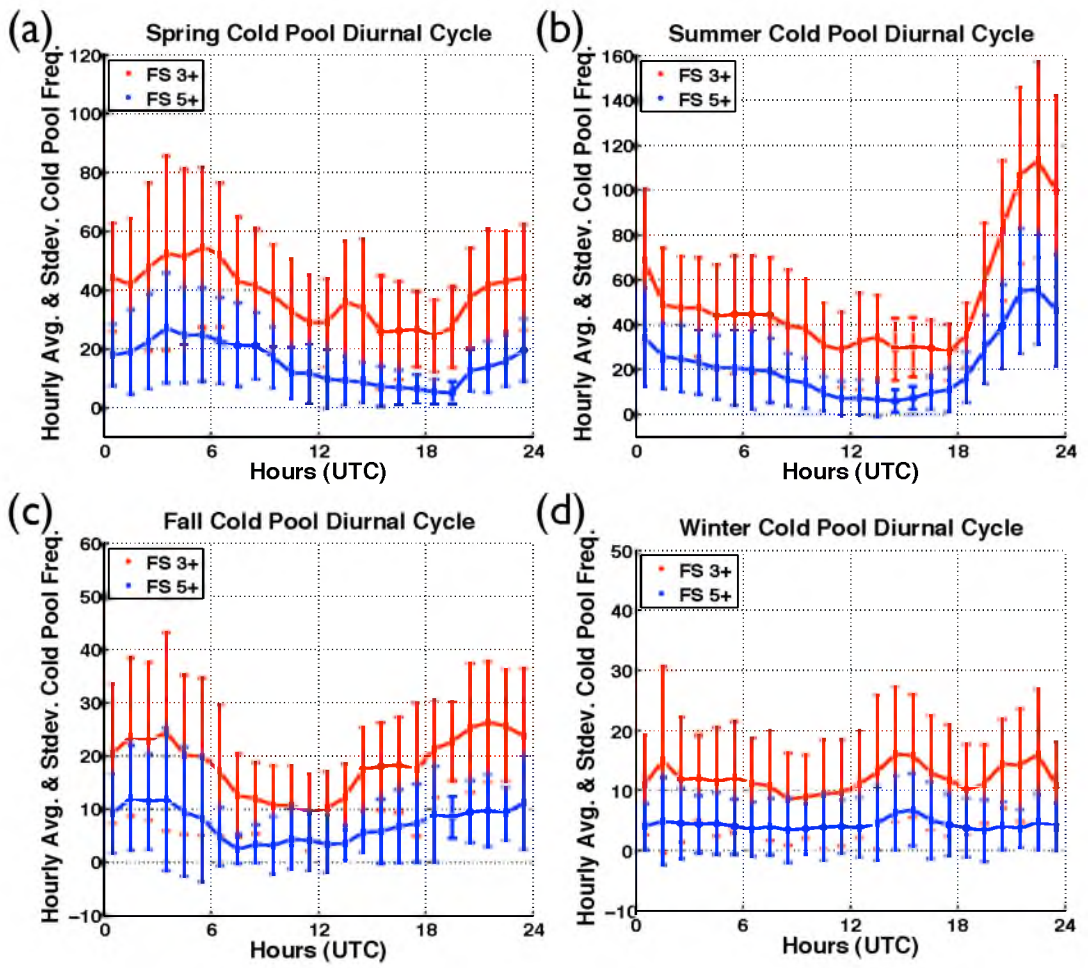

Figure 6.3 – Seasonally averaged diurnal cycle (in UTC time) of all cold pools at triangles in the Oklahoma Mesonet from the 1997-2011 period along with standard deviations. Results are shown for (a) spring, (b) summer, (c), fall, and (d) winter for all frontal passages which yielded cold pools (red) and strong frontal passages which yielded cold pools (blue).

frontal passage frequency on the area and maximum side length of the triangle. For this reason, triangles with side lengths > 80 km, which were located primarily along the outer boundary, were dropped from the Delaunay triangulation grid and are not used in any of the results detailed throughout this work. As a result, 10-13 stations a year were removed due to the side length issue from the 99-104 original stations that met the observation threshold. Linear regressions of the remaining triangles were performed using a least-squares fit to determine the dependence on triangle area (Fig. 6.5) and maximum side length (Fig. 6.6).

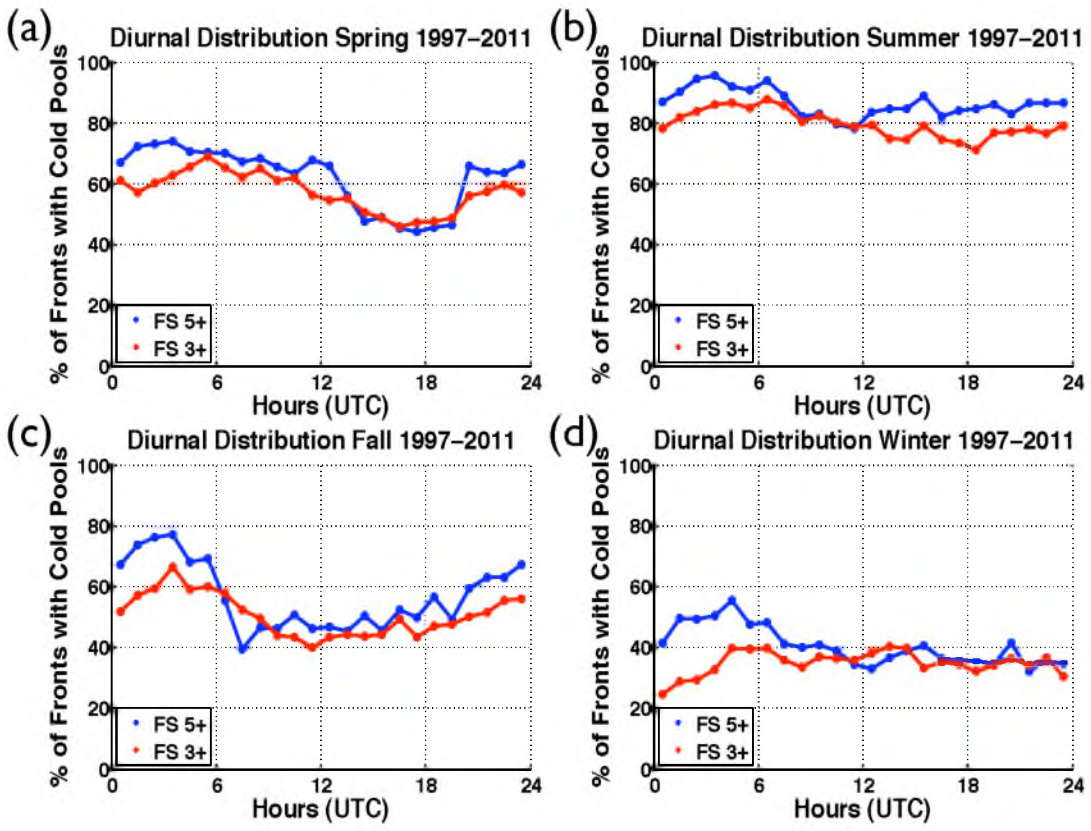

Figure 6.4 – Seasonally averaged diurnal cycle (in UTC time) of the percentage of all (red) and strong (blue) fronts that yield cold pools. Results are shown for (a) spring, (b) summer, (c), fall, and (d) winter for all frontal passages (red) and strong frontal passages (blue).

Smaller triangles and triangles with shorter maximum side lengths had lower frequencies of frontal passages and cold pool occurrence on average. This was expected since all three triangle corners had to be activated to trigger a frontal passage. With small, isolated thunderstorm events this is less likely to be captured on portions of the grid with lower resolution, as well as very slow moving storms that failed to reach all three corners within 2 hrs. The following equations (Eq. 6.1-6.8) are the results of the linear fits for fronts and cold pools:

$$Fronts_{\mathrm{FS3+}} = -7.5\mathrm{E}^{-3} \times \mathrm{TriangleArea} + 34 \tag{6.1}$$

$$Fronts_{\mathrm{FS5+}} = -3.1\mathrm{E}^{-3} \times \mathrm{TriangleArea} + 13 \tag{6.2}$$

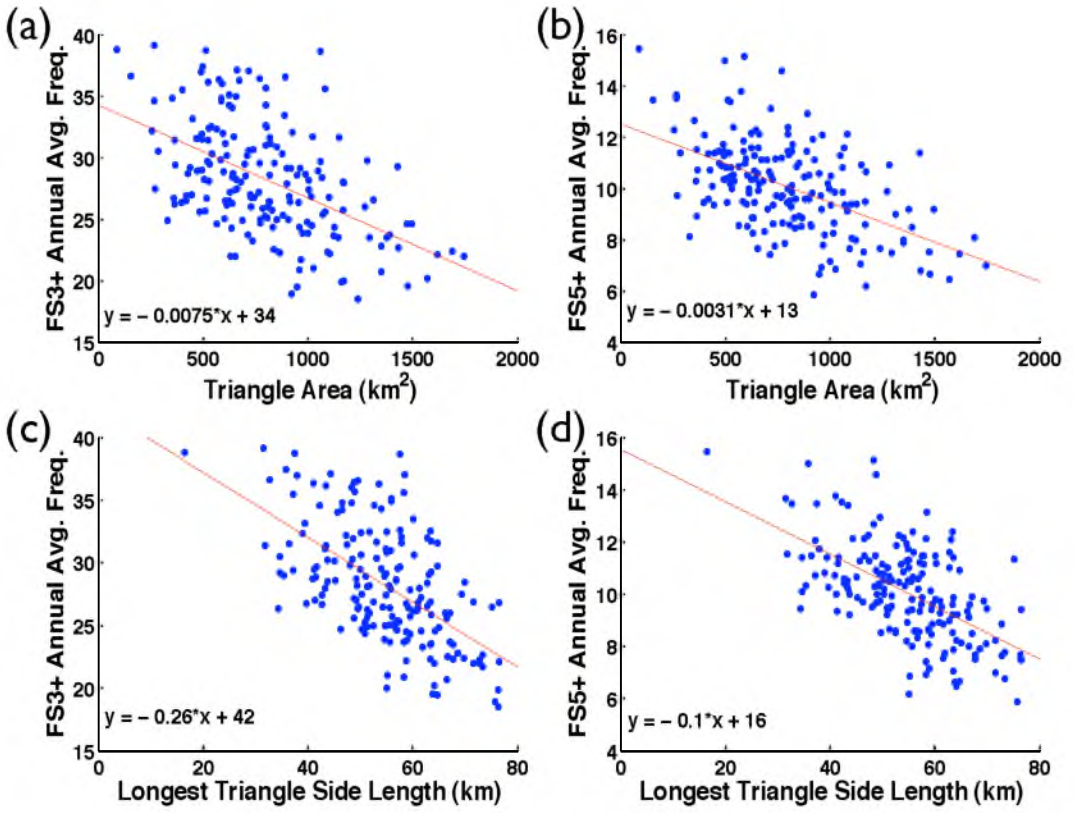

Figure 6.5 – Scatterplots with linear regression lines for (a) annually averaged frontal passage frequency and Mesonet triangle area, (b) annually averaged strong frontal passage frequency and Mesonet triangle area, (c) annually averaged frontal passage frequency and longest Mesonet triangle side length, and (d) annually averaged strong frontal passage frequency and longest Mesonet triangle side length.

$$Fronts_{\mathrm{FS3+}} = -0.26 \times TriangleMaxSideLength + 42 \tag{6.3}$$

$$Fronts_{\mathrm{FS5+}} = -0.10 \times TriangleMaxSideLength + 16 \tag{6.4}$$

$$ColdPools_{\mathrm{FS3+}} = -1.1\mathrm{E}^{-2} \times \mathrm{TriangleArea} + 25 \tag{6.5}$$

$$ColdPools_{\mathrm{FS5+}} = -3.9\mathrm{E}^{-3} \times \mathrm{TriangleArea} + 10 \tag{6.6}$$

$$ColdPools_{\mathrm{FS3+}} = -0.26 \times TriangleMaxSideLength + 31 \tag{6.7}$$

$$ColdPools_{\mathrm{FS5+}} = -0.10 \times TriangleMaxSideLength + 12 \tag{6.8}$$

Each triangle was adjusted using these regression lines by assuming all triangles had the average area and side length and moving the scatterplot point value along a

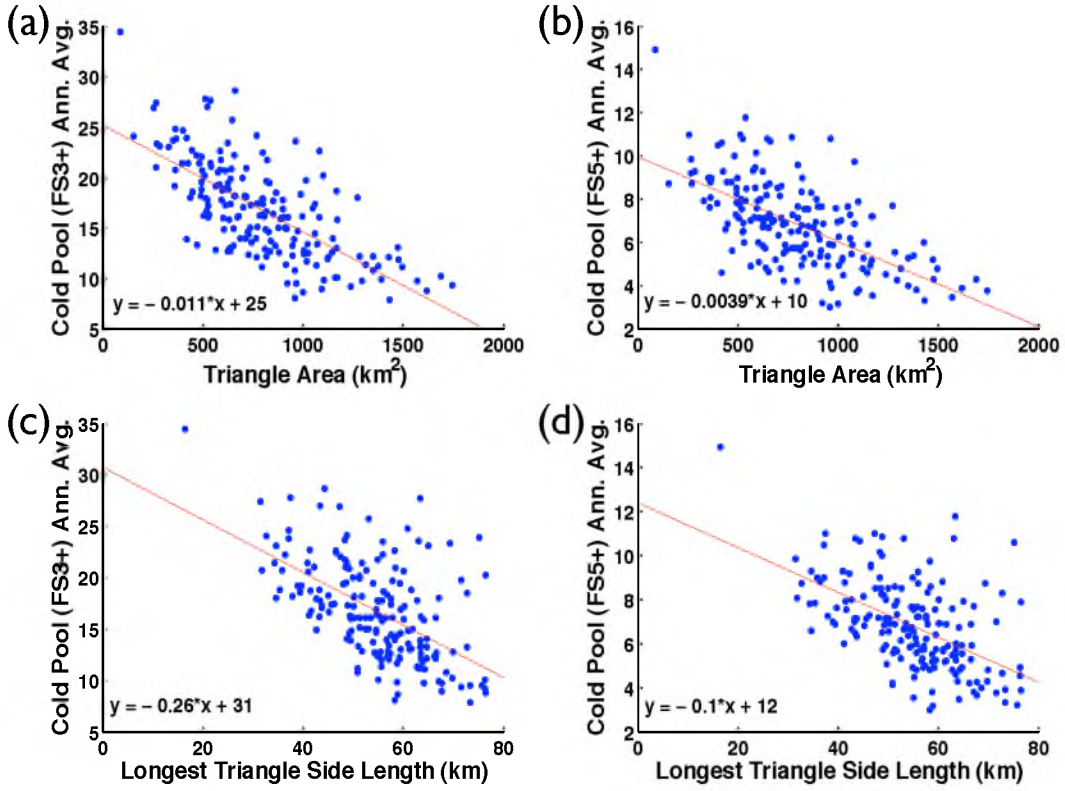

Figure 6.6 – Scatterplots with linear regression lines for (a) annually averaged cold pool frequency and Mesonet triangle area, (b) annually averaged strong cold pool frequency and Mesonet triangle area, (c) annually averaged cold pool frequency and longest Mesonet triangle side length, and (d) annually averaged strong cold pool frequency and longest Mesonet triangle side length.

line with the same slope as the regression line. The end result of this adjustment is the geographic distributions of fronts (Fig. 6.7) and cold pools (Fig. 6.8) displayed. Points on these plots are station centroids for triangles that were present in the Mesonet for over 5 yrs with the size of the point scaled by the number of years that the point is a centroid (max: 15). Since some stations are either removed from the Mesonet, fail to meet the observation threshold for a year, or are moved to a different location, the triangles are not constant. The grid applies to the 1997 data; points that are not centroids of these triangles are centroids for triangles that are present later in the dataset.

For the frontal passages adjusted by area (Fig. 6.7a) a clear west to east gradient is apparent with western regions of Oklahoma observing larger frequencies of frontal

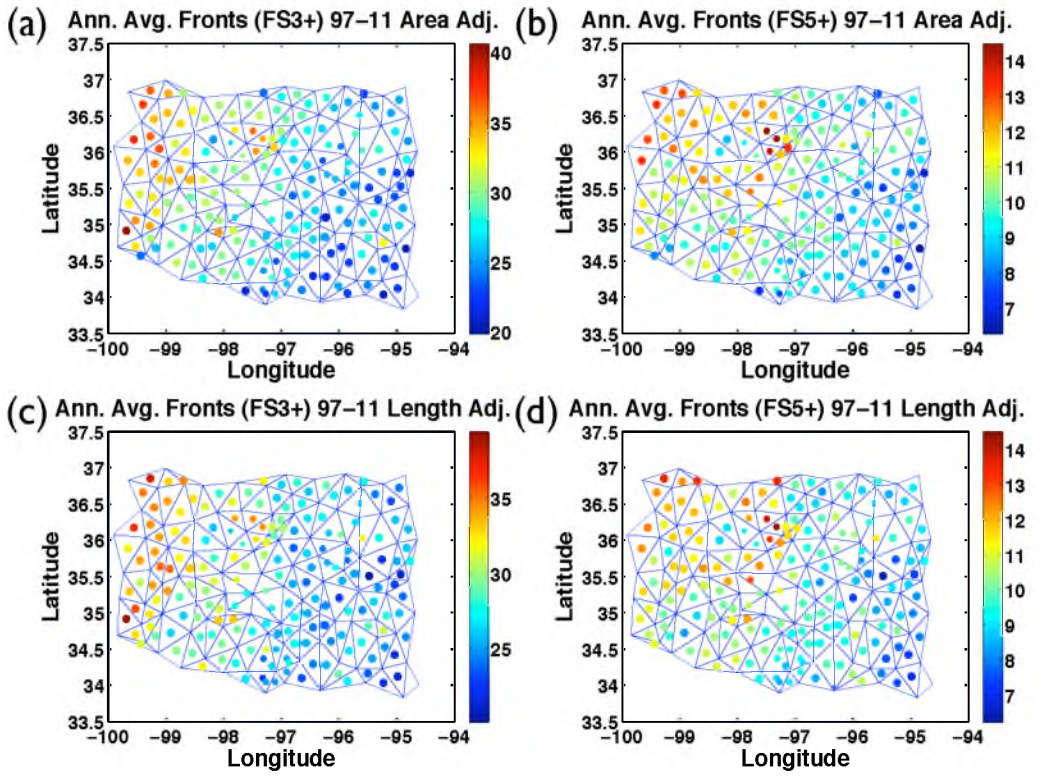

Figure 6.7 – Geographic distribution of (a) all frontal passages, adjusted for triangle area, (b) strong frontal passages, adjusted for triangle area, (c) all frontal passages, adjusted for maximum triangle side length, and (d) strong frontal passages, adjusted for maximum triangle side length. Size of dots represents the number of years the triangle centroid was at that location (1997-2011). Only triangles that were present more than 5 years are shown. The grid is the 1997 triangles; since the grid can change each year the 1997 grid is only a close representation.

passages than eastern regions of Oklahoma. Skinny triangles along the borders (ones that remained in the grid) appear to still underestimate the number of frontal passages that occur, even after the area adjustment. The triangle with the highest frequency of frontal passages before the adjustment is the small triangle in the north central part of the state. After the adjustment this triangle has a lower frequency than the stations to its west. Strong fronts adjusted by area (Fig. 6.7b) show a similar distribution with only minor differences. The southwestern corner appears to have a lower frequency of strong fronts relative to its value for total fronts. Also, the stations in the north central region have the highest rates of strong fronts.

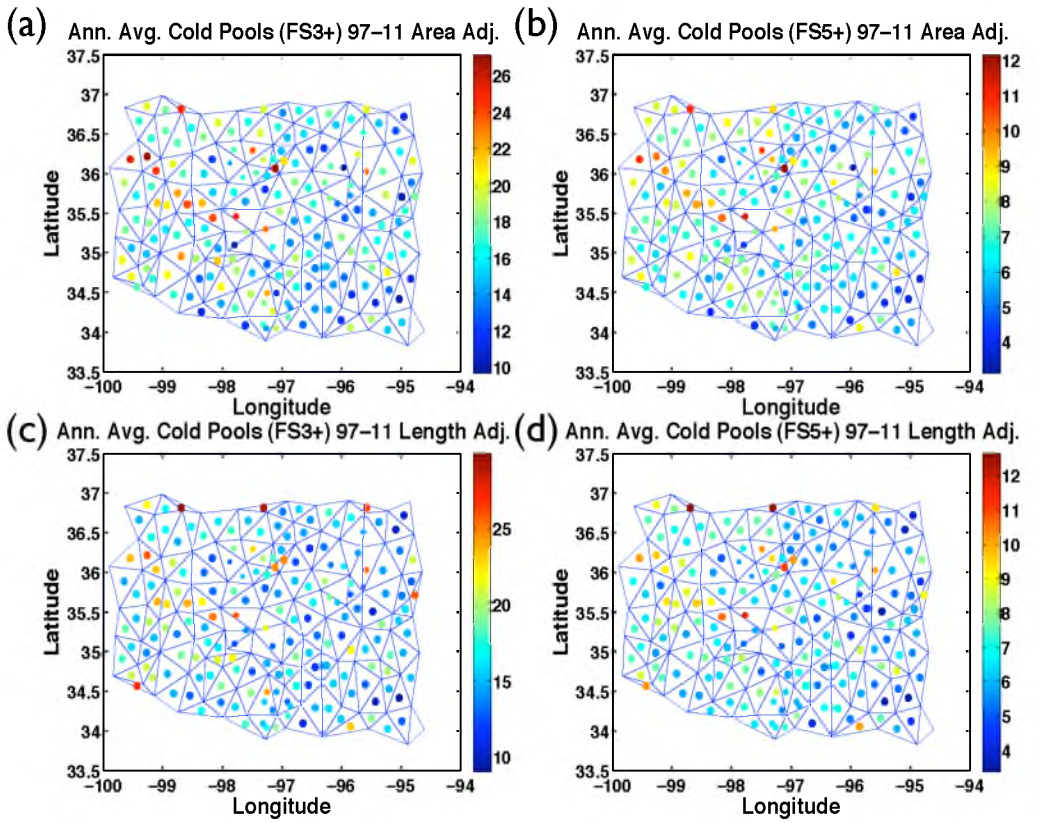

Figure 6.8 – Geographic distribution of (a) all fronts which yield cold pools, adjusted for triangle area, (b) strong fronts which yield cold pools, adjusted for triangle area, (c) all fronts which yield cold pools, adjusted for maximum triangle side length, and (d) strong fronts which yield cold pools, adjusted for maximum triangle side length. Size of dots represents the number of years the triangle centroid was at that location (1997-2011). Only triangles that were present more than 5 years are shown. The grid is the 1997 triangles; since the grid can change each year the 1997 grid is only a close representation.

For frontal passages adjusted by maximum side length (Fig. 6.7c) the same west to east pattern remains. The main difference between the area adjustment and the length adjustment is that for skinny triangles the length adjustment yields a much higher frequency value than the area adjustment. Additionally, roughly equilateral triangles have a lower frequency value with the length adjustment than the area adjustment. This is the case for all frontal passages and for the strong frontal passages (Fig 6.7d).

For cold pools adjusted for area the west to east gradient is much weaker than it is for frontal passages (Fig. 6.8a). West-central Oklahoma appears to have a narrow

filament of higher than average frequencies of cold pool occurrence. The northwest and southwest have lower average frequencies of cold pools compared to state average than they have frontal passages. Cold pools from strong fronts (Fig. 6.8b) show roughly the same pattern. Cold pools adjusted for length instead of area (Fig. 6.8c, 6.8d) show the same differences compared to area as was the case for frontal passages. The border edge skinny triangles have the highest rates of cold pools after the adjustment. It would appear at a glance that area is the more accurate adjustment of the two when it comes to cold pools.

The distribution of the difference between means for each station relative to the Mesonet average was calculated for stations that were present more than 5 of the 15 yrs. The Mesonet average compared to a station would only include the years in which that station was part of the Mesonet average. The Student t-scores were calculated for four sets of data: (1) the original grid, (2) an adjusted grid that removed triangles with maximum triangle side length > 80 km, (3) the adjusted grid with the frequencies adjusted for triangle area, and (4) the adjusted grid with the frequencies adjusted for maximum triangle side length with the average t-score magnitude shown (Table 6.8). For sample sizes of 6-15 yrs, t-scores > 2.447 (for 6 yrs) and > 2.131 (for 15 yrs) are statistically different than the Mesonet average at the 95% confidence level.

For the unadjusted grid, frontal passages average t-scores were 2.18 and 1.61 for all fronts and strong fronts respectively. The average t-score is much higher for cold pools, at 3.36 and 2.26 for all cold pools and cold pools associated with strong fronts. When the extra-long triangles above 80 km in side length are removed the t-scores decrease in magnitude roughly 10% for fronts and a smaller decrease for cold pools. The adjustments for area and length significantly reduced the magnitude of the t-scores. This shows that both area and side length play a role in causing triangles to overestimate or underestimate the frequency of frontal passages. For all grids and adjustments the strong fronts and cold pools following strong fronts had lower t-scores than for all fronts and cold pools. The average magnitude of the t-score for frontal passages was lower with the length adjustment than with the area adjustment. However, the average magnitude of the t-score for cold pools was lower

Table 6.8 – Average magnitude of Student t-scores from distribution of difference between mean scores for triangles that were present in the Mesonet for over 5 years. Values are given for fronts and cold pools of both strengths. The Original column contains the t-scores for the original grid. The Grid column refers to t-scores for the grid adjusted to remove triangles with too-large side lengths. The final two columns have the t-scores with the grid adjustment and the area and triangle side length adjustments, respectively.

Adjustments	**Original**	**Grid**	**Grid & Area**	**Grid & Length**
Fronts (FS3+)	2.18	1.90	1.58	1.47
Fronts (FS5+)	1.61	1.37	1.10	1.06
Cold Pools (FS3+)	3.36	3.27	2.21	2.62
Cold Pools (FS5+)	2.26	2.13	1.60	1.74

with the area adjustment than with the length adjustment. Also, frontal passages had lower average t-scores than cold pools for all grids and adjustments.

CHAPTER 7

DISCUSSION

The results detailed in the preceding chapters extend analysis of Oklahoma Mesonet data to a 15-yr dataset, providing a much larger sample size for seasonal analyses of frontal passages and convective cold pools. This allows for clearer signals to appear in the data with increased certainty that the results obtained here are representative.

7.1 Research Findings

There was a maximum correlation between updrafts and downdrafts with precipitation during the summer months with a minimum correlation in winter (Table 4.1). Convective precipitation from cumulonimbus clouds is more prevalent in the summer as a result of daytime convective heating leading to the generation of late afternoon and evening thunderstorms and squall lines. This increase in convective precipitation is evident by the increased frequency of frontal passages and cold pools in the diurnal pattern during the summer months (Fig. 6.2-6.3). Additionally, there is more moisture in the atmosphere during the summer which can lead to heavier precipitating storms. As a result, strong updrafts and downdrafts feature more prominently alongside the summertime convection, which leads to a more distinct and correlated updraft-downdraft couplet. In the winter, due to the colder temperatures, moisture levels are much lower. Updrafts and downdrafts that tend to be weaker lead to a larger proportion of precipitation that is stratiform. The weaker updrafts and downdrafts result in a less prominent couplet and reduced correlation.

However, other correlations decreased during the summer relative to the other seasons, such as most of the correlations between ΔT, ΔP, Δq_v, and $\Delta h c_p^{-1}$ (Tables 6.1 and 6.2). The correlation between ΔT and Δq_v was even slightly negative for the summer when it was positive for the other seasons. The correlation of ΔT with ΔP

was near 0 during the summer with -0.04 for strong summer fronts that led to cold pools. This suggests that the vertical structure of the temperature perturbation in the cold pools varies significantly from case to case. The variations in structure are expected to be larger in convective systems rather than in stratiform precipitation systems due to deeper and more varied updraft, boundary layer, and cold pool heights. Three-dimensional data would aid in resolving the vertical features in the Mesonet. For this reason, case studies involving intense observations periods (IOPs) are the most productive to pursue in future research. The MC3E period is one such IOP that would have an enhanced capacity to resolve 3D structure for cases.

Frontal passages and cold pools generally had similar statistics for changes between variables and correlations. However, Δq_v and $\Delta h c_p^{-1}$ had slightly larger values for cold pools (roughly 10%) than for all frontal passages though the seasonal pattern remained the same. This is likely a result of the tendency of dry frontal passages to not have cold pools due to a lack of strong divergence behind those fronts. The lack of precipitation in dry frontal passages would reduce the magnitude of the ensuing q_v fall which in turn reduces the magnitude of the hc_p^{-1} decrease.

7.2 Comparisons to Previous Studies

Some of the statistics that gained a much larger sample size relative to previous work were the correlations between updrafts and downdrafts with precipitation. Sun and Krueger (2012) in their Figure 5 showed correlations that peaked slightly higher for MJJA 1997 than for the JJA period for the 15 yrs of Mesonet data. Their peak correlations were roughly 0.6 for M_u with precipitation and M_d with precipitation, 0.65 for M_u^+ with precipitation, and 0.7 for M_d^+ with precipitation whereas the JJA period in the 15-yr dataset had correlations of 0.48, 0.55, and 0.59, respectively. Also, their M_d and M_d^+ values lagged precipitation and the updrafts by an hour. However, the 1997-2011 analysis in this study used 3-hr averaging which would likely smooth out the expected maximum correlations making the results roughly the same between the 15-yr Mesonet dataset and the Sun and Krueger analysis as would be expected.

Studies have observed pressure and temperature changes in cold pool cases. In one such study (Engerer et al., 2008) the average pressure rise in cold pools from 39

MCS events between April and August was 4.5 mb while the average temperature fall was 9.5 K. It is safe to assume that these MCS events were chosen because they were particular strong so the comparison for the 15-yr dataset would be strong fronts which averaged a 3.6-mb pressure rises in spring, a 2.5-mb pressure rises in summer, and a 7.7-K temperature drops in both spring and summer. Though the Engerer et al. study found larger pressure and temperature changes on average, considering the that 15-yr dataset was diurnally adjusted, and the much larger sample size for 15-yr dataset of strong fronts that may be weighted down with weaker, albeit still strong, fronts, the results are in reasonable agreement.

Cold pools in this study were similar to other studies in terms of the length of a cold pool along the front that can form in the 100s of km. However, the width a cold pool extended back from the lead storm axis was typically on the order of 50-100km while in other studies the distance can be 100-400 km for MCS cases (Stensrud et al., 1999). Additionally, in the case studies described in Chapter 5 most triangles held a cold pool for around 30-60 mins while there are other studies that have mean lifetimes of multiple hours (Tompkins, 2001; Young and Perugini, 1995).

The geographical distribution of frontal passages suggests a west to east gradient with a higher frequency of frontal passages on the westward side of Oklahoma. One likely influence is the dryline which frequently develops in the lee of the Rocky Mountains and advances into Oklahoma where numerous case studies have been made over the years (McCarthy and Koch, 1982; Ziegler and Hane, 1993; Buban et al., 2007). A climatology of springtime dryline position matches well with the frontal passage geographic distribution anomaly pattern (Hoch and Markowski, 2005). Their Fig. 2 showed that the dryline most frequently was located around 101W longitude and the dryline location range is generally from 103W to 97W near Oklahoma City with rare occurrences farther eastward. The west to east pattern is weaker when it comes to cold pools, suggesting that western stations have a higher rate of frontal passages not resulting in cold pools.

CHAPTER 8

CONCLUSIONS

8.1 Summary of Results

A 15-yr climatology of Oklahoma Mesonet mass flux estimates, frontal passages, and cold pools was created and analyzed. Previous studies involving cold pools in the Oklahoma Mesonet have looked at shorter time periods, with a focus on other features such as MCSs (Engerer et al., 2008) and squall lines (Adams-Selin and Johnson, 2010).

For Oklahoma Mesonet gridded triangles surface convergence and divergence were calculated as a proxy for near-cloud-base convective mass fluxes. Regions of convergence, divergence, strong convergence, and strong divergence (strong referring to regions with magnitudes $> 10^{-4}\text{s}^{-1}$ only) were summed and divided over the entire Mesonet domain as the variables M_u, M_d, M_u^+, and M_d^+, respectively. The largest M_u, M_d, M_u^+, and M_d^+ values, on average, were during the spring, while the smallest were during the winter. The annual pattern was fairly consistent from year to year. Correlations were calculated between convergence, divergence, and precipitation for 3-hr averages. There were higher correlations in the summer and lower correlations in the winter. M_u^+ and M_d^+ had higher correlations with each other and precipitation than M_u and M_d had with each other and precipitation. Average M_u^+ and M_d^+ values were calculated for wet (Mesonet area averaged precipitation > 1 mm) and dry (0 precipitation) days. Wet spring and summer days had the largest convergence and divergence while dry summer and fall days had the smallest convergence and divergence.

Frontal passages were calculated by identifying when Mesonet stations experienced a front. A nondimensional variable, the front score (FS), was derived using 30-min temperature falls and pressure rises. When all three stations in a Mesonet triangle experience a frontal passage within 2 hrs a front occurs at the Mesonet triangle and

can be tracked. A cold pool requires a frontal passage to occur at a Mesonet triangle and for the divergence of the triangle to exceed the threshold value of $> 10^{-4}\text{s}^{-1}$ within half an hr before or an hr after the frontal passage is halfway through the triangle.

Frontal passages and cold pools were examined in detail for several case studies, of which four were outlined here: 1) 13 June 1997, 2) 15-16 June 2002, 3) 20 May 2011 and 4) 24-25 May 2011. These fronts were captured quite well as they progressed through the Oklahoma Mesonet. Even some finer details were picked up such as weaknesses in the line, represented by lower front scores and weaker convergence-divergence gradients across the front. An example of the influences of different storm systems was the 24-25 May 2011 case during which a tornado outbreak occurred. This system lacked the strong convergence-divergence gradient the other case studies yielded, suggesting that the strong rotation in the system might have reduced the strength and/or size of the divergence behind the front. Cold pool extents and longevity varied from case to case.

The frontal passage and cold pool results suggested a tendency for dry synoptic scale fronts to not be associated with areas of strong divergence. Alternatively, fronts associated with MCSs resulted in precipitation and a mesoscale divergence region at the surface. However, there are exceptions to both types in the analysis leaving this differentiation short of being a rule.

Changes in temperature (T), pressure (P), water vapor mixing ratio (q_v), and moist static energy in temperature units (hc_p^{-1}) during frontal passages were computed. Frontal passages, with or without cold pools, had smaller magnitudes of ΔP, Δq_v, and Δhc_p^{-1} during the summer season than in other seasons. Spring had the smallest magnitudes of ΔT. Winter had the largest magnitudes, with the exception of Δq_v, which were slightly larger in spring and fall. Correlations involving ΔT were lowest in the summer and highest during the winter except for strong spring frontal passage ΔT correlations with ΔP. Correlations with ΔP and Δq_v or Δhc_p^{-1} were lowest in the summer and winter. The correlations between Δq_v and Δhc_p^{-1} were above 0.9 year-round. Of particular note is the negative correlation between ΔT and Δq_v during the summer and the positive correlation between ΔP and Δq_v for

strong winter frontal passages, contrary to the sign in those correlations for the other seasons. The Δ averages and their correlations were generally similar for cold pool producing fronts and for all fronts.

Seasonally, summer has the highest frequency of frontal passages and cold pools with spring second. Summer has the highest percentage of frontal passages with cold pools. Winter was lowest in all of these categories. The diurnal cycle of fronts and cold pools has a strong seasonal variation. During the summer, frontal passages and cold pools are most frequent in the late afternoon to evening hours, coinciding with daytime-heating-induced convection. The other seasons have much smaller variation in frontal passage and cold pool frequency in the diurnal cycle. The summer pattern is the dominant influence on the annual pattern for the diurnal cycle.

Geographically, the size of Mesonet triangles, in terms of area and maximum side length, has a significant influence on the analyzed frequency of frontal passages and cold pools. After this analysis artifact is accounted for, it is evident that western regions of Oklahoma experienced higher frequencies of frontal passages in particular, and cold pools to a lesser degree, than eastern regions. Difference between means student t-scores were calculated for each Mesonet triangle relative to the Mesonet average for front and cold pool annual frequency. A lower t-score magnitude means a station is closer to the Mesonet average and less likely to be statistically significantly different from that average. Frontal passages had lower differences between means Student t-score magnitudes from station to Mesonet average than cold pools. However, the area adjustment led to lower average t-score magnitudes for cold pools than the length adjustment, while the length adjustment led to lower average t-score magnitudes for frontal passes than the area adjustment. This suggests that the area adjustment is the more representative adjustment for cold pools while the length adjustment is the more representative adjustment for frontal passages.

8.2 Future Research Possibilities

This research could be expanded in the future by evaluating these methods with simulations using models such as WRF (Weather Research and Forecasting) and SAM (System for Atmospheric Modeling). Particularly useful would be the increased

resolution in a model relative to the Oklahoma Mesonet. A higher resolution would improve representations, especially for cases of smaller scale features and isolated convection that can be missed on grids with 40-km spacing.

Additionally, the Mesonet observations resided in only two spatial dimensions, so obtaining three-dimensional data, whether observationally or with model output, will help better understand the reasons behind the low correlations between changes in variables during summer frontal passages. The MC3E field campaign produced an extensive set of data which could be used for case study analyses in three dimensions.

Another possibility is to incorporate more variables into the front and cold pool detection methods. Wind shifts mark frontal passages and could be included in the front score calculation as well rather than just looking at temperature and pressure. Another option for frontal passages is to use potential temperature rather than temperature as has been done previously (Engerer et al., 2008).

Precipitation is necessary for evaporative cooling, though the precipitation does not have to reach the ground for evaporative cooling to occur. Including precipitation and any divergence (rather than half-max divergence) as factors keeping a cold pool active could better represent total cold pool area.

Estimating rain evaporation from surface pressure anomalies in cloud-resolving model simulations could be used to develop a method that could be implemented in cold pool analysis. Fujita had developed methods to calculate rain evaporation which assumed that the entirety of the pressure rise was a result of evaporated precipitation (Fujita, 1959). Comparing such estimated rain evaporation to actual rain evaporation in cloud-resolving model (CRM) simulations can better identify the method best suited for developing rain evaporation estimates using only surface observations.

Additionally, these results could be used to evaluate cold pool parameterizations in GCMs. Identifying regions of cold air production at the surface due to precipitation evaporation and surface outflow boundaries could lead to an improved predictability in new cell formation, cold pool longevity, and other structures.

Furthering the understanding of cold pools could lead to better representation of them in numerical weather prediction models, as well as improved analysis of gust fronts, squall lines, MCSs, and other features associated with convection. Improved

tracking of mesoscale and synoptic conditions, in turn, would lead to increased preparedness when it comes to severe weather events.

REFERENCES

Adams-Selin, R. D. and R. H. Johnson, 2010: Mesoscale surface pressure and temperature features associated with bow echoes. *Mon. Wea. Rev.*, **138**, 212–227.

Arakawa, A. and W. H. Schubert, 1974: Interaction of a cumulus cloud ensemble with the large-scale environment, Part I. *J. Atmos. Sci.*, **31**, 674–701.

Brock, F. V., K. C. Crawford, R. L. Elliott, G. W. Cuperus, S. J. Stadler, H. L. Johnson, and M. D. Eilts, 1995: The Oklahoma Mesonet: A technical overview. *J. Atmos. Oceanic. Technol.*, **12**, 5–19.

Bryan, G. H. and M. D. Parker, 2010: Observations of a squall line and its near environment using high-frequency rawinsonde launches during VORTEX2. *Mon. Wea. Rev.*, **138**, 4076–4097.

Buban, M. S., C. L. Ziegler, E. N. Rasmussen, and Y. P. Richardson, 2007: The dryline on 22 May 2002 during IHOP: Ground-radar and in situ data analyses of the dryline and boundary layer evolution. *Mon. Wea. Rev.*, **135**, 2473–2505.

Corfidi, S. F., 2003: Cold pools and MCS propagation: Forecasting the motion of downwind-developing MCSs. *Wea. Forecasting*, **18**, 997–1017.

Crum, T. D., R. L. Alberty, and D. W. Burgess, 1993: Recording, archiving, and using WSR-88D data. *Bull. Amer. Meteor. Soc.*, **74**, 645–653.

Crum, T. D., R. E. Saffle, and J. W. Wilson, 1998: An update on the NEXRAD program and future WSR-88D support to operations. *Wea. Forecasting*, **13**, 253–262.

Davies-Jones, R., 1993: Useful formulas for computing divergence, vorticity, and their errors from three or more stations. *Mon. Wea. Rev.*, **121**, 713–725.

Dawson, D. T., II., M. Xue, J. A. Milbrandt, and M. K. Yau, 2010: Comparison of evaporation and cold pool development between single-moment and multimoment bulk microphysics schemes in idealized simulations of tornadic thunderstorms. *Mon. Wea. Rev.*, **138**, 1152–1171.

Droegemeier, K. K. and R. B. Wilhelmson, 1985a: Three-dimensional numerical modeling of convection produced by interacting thunderstorm outflows. Part I: Control simulation and low-level moisture variations. *J. Atmos. Sci.*, **42**, 2381–2403.

Droegemeier, K. K. and R. B. Wilhelmson, 1985b: Three-dimensional numerical modeling of convection produced by interacting thunderstorm outflows. Part II: Variations in vertical wind shear. *J. Atmos. Sci.*, **42**, 2404–2414.

Droegemeier, K. K. and R. B. Wilhelmson, 1987: Numerical simulation of thunderstorm outflow dynamics. Part I: Outflow sensitivity experiments and turbulence dynamics. *J. Atmos. Sci.*, **44**, 1180–1210.

Dubois, J. A. and P. L. Spencer, 2005: Computing divergence from a surface network: Comparison of the triangle and pentagon methods. *Wea. Forecasting*, **20**, 596–608.

Engerer, N. A., D. J. Stensrud, and M. C. Coniglio, 2008: Surface characteristics of observed cold pools. *Mon. Wea. Rev.*, **136**, 4839–4849.

Fujita, T., 1955: Results of detailed synoptic studies of squall lines. *Tellus*, **7**, 405–436.

Fujita, T., 1959: Precipitation and cold air production in mesoscale thunderstorm systems. *J. Meteor.*, **16**, 454–466.

Fulton, R. A., J. P. Breidenbach, D.-J. Seo, D. A. Miller, and T. O'Bannon, 1998: The WSR-88D rainfall algorithm. *Wea. Forecasting*, **13**, 377–395.

Grandpeix, J.-Y. and J.-P. Lafore, 2010: A density current parameterization coupled with Emanuel's convection scheme. Part I: The models. *J. Atmos. Sci.*, **67**, 881–897.

Grandpeix, J.-Y., J.-P. Lafore, and F. Cheruy, 2010: A density current parameterization coupled with Emanuel's convection scheme. Part II: 1D simulations. *J. Atmos. Sci.*, **67**, 898–922.

Grassotti, C., R. N. Hoffman, E. R. Vivoni, and D. Entekhabi, 2003: Multiple-timescale intercomparison of two radar products and rain gauge observations over the Arkansas-Red River Basin. *Wea. Forecasting*, **18**, 1207–1229.

Hoch, J. and P. M. Markowski, 2005: A climatology of springtime dryline position in the U.S. Great Plains region. *J. Climate*, **18**, 2132–2137.

Hohenegger, C. and C. S. Bretherton, 2011: Simulating deep convection with a shallow convection scheme. *Atmos. Chem. Phys.*, **11**, 10 389–10 406.

James, R. P., P. M. Markowski, and J. M. Fritsch, 2006: Bow echo sensitivity to ambient moisture and cold pool strength. *Mon. Wea. Rev.*, **134**, 950–964.

Knievel, J. C. and R. H. Johnson, 1998: Pressure transients within MCS mesohighs and wake lows. *Mon. Wea. Rev.*, **126**, 1907–1930.

Loehrer, S. M. and R. H. Johnson, 1995: Surface pressure and precipitation life cycle characteristics of PRE-STORM mesoscale convective systems. *Mon. Wea. Rev.*, **123**, 600–621.

Markowski, P. M. and Y. P. Richardson, 2012: *Mesoscale Meteorology in Midlatitudes.* Wiley-Blackwell, 407 pp.

McCarthy, J. and S. E. Koch, 1982: The evolution of an Oklahoma dryline. Part I: A meso- and subsynoptic-scale analysis. *J. Atmos. Sci.*, **39**, 225–236.

McPherson, R. A., et al., 2007: Statewide monitoring of the mesoscale environment: A technical update on the Oklahoma Mesonet. *J. Atmos. Oceanic Technol.*, **24**, 301–321.

Newton, C. W., 1950: Structure and mechanism of the prefrontal squall line. *J. Meteor.*, **7**, 210–222.

Qian, L., G. S. Young, and W. M. Frank, 1998: A convective wake parameterization scheme for use in general circulation models. *Mon. Wea. Rev.*, **126**, 456–469.

Rio, C., et al., 2012: Control of deep convection by sub-cloud lifting processes: The ALP closure in the LMDZ5B general circulation model. *Clim. Dynam.*, doi:10.1007/s00 382–012–1506–x.

Romero, R., C. A. Doswell III, and R. Riosalido, 2001: Observations and fine-grid simulations of a convective outbreak in Northeastern Spain: Importance of diurnal forcing and convective cold pools. *Mon. Wea. Rev.*, **129**, 2157–2182.

Rotunno, R., J. B. Klemp, and M. L. Weisman, 1988: A theory for strong, long-lived squall lines. *J. Atmos. Sci.*, **45**, 463–485.

Roux, F., 1988: The West African squall line observed on 23 June 1981 during COPT81: Kinematics and thermodynamics of the convective region. *J. Atmos. Sci.*, **45**, 406–426.

Schaefer, J. T., 1974: A simulative model of dryline motion. *J. Atmos. Sci.*, **31**, 956–964.

Seifert, A., 2008: On the parameterization of evaporation of raindrops as simulated by a one-dimensional rainshaft model. *J. Atmos. Sci.*, **65**, 3608–3619.

Seigel, R. B. and S. C. van den Heever, 2012: Simulated density currents beneath embedded stratified layers. *J. Atmos. Sci.*, **69**, 2192–2200.

Stensrud, D. J. and J. M. Fritsch, 1994: Mesoscale convective systems in weakly forced large-scale environments. Part II: Generation of a mesoscale initial condition. *Mon. Wea. Rev.*, **122**, 2068–2083.

Stensrud, D. J., G. S. Manikin, E. Rogers, and K. E. Mitchell, 1999: Importance of cold pools to NCEP mesoscale Eta model forecasts. *Wea. Forecasting*, **14**, 650–670.

Stoelinga, M. T., J. D. Locatelli, R. D. Schwartz, and P. V. Hobbs, 2003: Is a cold pool necessary for the maintenance of a squall line produced by a cold front aloft? *Mon. Wea. Rev.*, **131**, 95–115.

Stumpf, G. J., R. H. Johnson, and B. F. Smull, 1991: The wake low in a midlatitude mesoscale convective system having complex convective organization. *Mon. Wea. Rev.*, **119**, 134–158.

Sud, Y. C. and G. K. Walker, 1993: A rain evaporation and downdraft parameterization to complement a cumulus updraft scheme and its evaluation using GATE data. *Mon. Wea. Rev.*, **121**, 3019–3039.

Sun, R. and S. K. Krueger, 2012: Mesoanalysis of the interactions of precipitating convection and the boundary layer. *J. Adv. Model. Earth Syst.*, **4**, M04004.

Tepper, M., 1950: A proposed mechanism of squall lines: The pressure jump line. *J. Meteor.*, **7**, 21–29.

Tompkins, A. M., 2001: Organization of tropical convection in low vertical wind shears: The role of cold pools. *J. Atmos. Sci.*, **58**, 1650–1672.

Wakimoto, R. M., 1982: The life cycle of thunderstorm gust fronts as viewed with Doppler radar and rawinsonde data. *Mon. Wea. Rev.*, **110**, 1060–1082.

Wallace, J. M. and P. V. Hobbs, 2006: *Atmospheric Science: An Introductory Survey. 2nd ed.* Academic Press., 483 pp.

Weisman, M. L., 2001: Bow echoes: A tribute to T. T. Fujita. *Bull. Amer. Meteor. Soc.*, **82**, 97–116.

Weisman, M. L. and R. Rotunno, 2005: Reply. *J. Atmos. Sci.*, **62**, 2997–3002.

Weiss, C. C. and H. B. Bluestein, 2002: Airborne pseudo-dual Doppler analysis of a dryline-outflow boundary intersection. *Mon. Wea. Rev.*, **130**, 1207–1226.

Wilhelmson, R. B. and C.-S. Chen, 1982: A simulation of the development of successive cells along a cold outflow boundary. *J. Atmos. Sci.*, **39**, 1466–1483.

Wilhelmson, R. B. and J. B. Klemp, 1978: A numerical study of storm splitting that leads to long-lived storms. *J. Atmos. Sci.*, **35**, 1974–1986.

Young, G. S. and S. M. Perugini, 1995: Convective wakes in the equatorial western Pacific during TOGA. *Mon. Wea. Rev.*, **123**, 110–123.

Ziegler, C. L. and C. E. Hane, 1993: An observational study of the dryline. *Mon. Wea. Rev.*, **121**, 1134–1151.